Chelating agent effects in the synthesis of supported Ni nanoparticles as catalysts for hydrogen production

Alejandra C. Villagran-Olivares[a*], Manuel F. Gomez[a], Carlos A. López[a], Jordi Llorca[b], Mariana N. Barroso[a], María C. Abello[a]

[a] *Instituto de Investigaciones en Tecnología Química (INTEQUI-CONICET-UNSL), Facultad de Química, Bioquímica y Farmacia. Almirante Brown 1455, 5700, San Luis, Argentina.*
[b] *Instituto de Técnicas Energéticas, Departamento de Ingeniería Química, Universitat Politècnica de Catalunya, EEBE, 08019, Barcelona, Españа.*

Abstract

A series of Ni supported over $MgAl_2O_4$-CeO_2 catalysts have been prepared by the wet impregnation method as catalysts for steam ethanol reforming. The synthesis was performed using nitrilotriacetic acid (NTA) or citric acid (CA) as chelating agents (L) with different L/Ni ratios. The features of catalytic solids were determined by DR-UV-Vis-NIR, FTIR, BET, TGA, XRD, H_2-TPR, XPS, Raman, HRTEM and SEM. Changes in the crystallite size of NiO and CeO_2 were evidencied with the use of NTA, while the addition of CA allowed to reduce the crystallite size of NiO and Ni with a slight effect in CeO_2 size. The use of chelating agents induced changes in the Ni-CeO_2 interactions and an increase in the Ce/Ni^0 surface ratio. Catalytic systems prepared using a L/Ni ratio leading to the most stable complex formation (NTA/Ni=1 and CA/Ni=2) exhibited the best performances in the reforming reaction under the operation conditions studied.

Keywords: Nano-Ni catalysts, Chelating agent, Nitrilotriacetic acid, Citric acid, Hydrogen, Ethanol steam reforming

1. Introduction

Ethanol steam reforming (ESR) is a potential sustainable hydrogen production process and it has been extensively studied over non-noble transition metal catalysts because they are less expensive than the noble metal ones. In particular, Ni catalysts are preferred because Ni dissociates C-C bonds more efficiently than Co [1-3]. ESR is an endothermic process, which produces 6 mol of hydrogen and 2 mol of carbon dioxide if only ocurrs reforming reaction (equation 1). However, other reactions usually ocurrs such as ethanol dehydrogenation, acetaldehyde steam reforming, ethanol dehydratation, ethanol decomposition, acetaldehyde decomposition, water gas shift reaction, ethylene decomposition, methane decomposition and Boudouard reaction (equations 2-10) [1]:

$$C_2H_5OH\,(g) + 3\,H_2O\,(g) \rightarrow 2\,CO_2\,(g) + 6\,H_2\,(g) \qquad \Delta H^0_{298K} = +173.5\ kJ/mol \qquad \Delta H^0_{923K} = +206.4\ kJ/mol \qquad (1)$$

$$C_2H_5OH\,(g) \rightarrow C_2H_4O\,(g) + H_2\,(g) \qquad \Delta H^0_{298K} = +68.9\ kJ/mol \qquad (2)$$

$C_2H_4O\ (g) + H_2O\ (g) \rightarrow 2\ CO\ (g) + 3\ H_2\ (g)$ $\Delta H^0_{923K} = +186.8$ kJ/mol (3)

$C_2H_5OH\ (g) \rightarrow C_2H_2\ (g) + H_2O\ (g)$ $\Delta H^0_{298K} = +45.5$ kJ/mol (4)

$C_2H_5OH\ (g) \rightarrow CO\ (g) + CH_4\ (g) + H_2\ (g)$ $\Delta H^0_{298K} = +49.6$ kJ/mol (5)

$C_2H_4O\ (g) \rightarrow CH_4\ (g) + CO\ (g)$ $\Delta H^0_{298K} = -19.3$ kJ/mol (6)

$CO\ (g) + H_2O\ (g) \leftrightarrow CO_2\ (g) + H_2\ (g)$ $\Delta H^0_{298K} = -41.4$ kJ/mol (7)

$C_2H_4\ (g) \rightarrow 2\ C\ (s) + 2\ H_2\ (g)$ $\Delta H^0_{298K} = -52.3$ kJ/mol (8)

$CH_4\ (g) \rightarrow 2\ H_2\ (g) + C\ (s)$ $\Delta H^0_{298K} = +74.9$ kJ/mol (9)

$2\ CO\ (g) \leftrightarrow CO_2\ (g) + C\ (s)$ $\Delta H^0_{298K} = -172.6$ kJ/mol (10)

The occurrence of these reactions mainly depends on the properties of catalyst and operation conditions. One of the disadvantages of the secondary reactions over Ni catalysts is the deactivation by carbon deposition, sintering and active phase oxidation [4]. Ethylene decomposition, Boudouard reaction and methane decomposition are the main routes to carbon deposition [1-3, 5]. However, there is no linear relationship between the decrease in catalyst activity and the coke content [5]. These phenomena of deactivation are the main technological obstacles in today's reformers. This goal could be achieved by Ni particles below a critical size, which would be allowed to develop an active, selective and stable catalyst. As in the methane reforming the control of metal assembly size in the ESR has the same objective: to increase dispersion and decrease carbon deposition by inhibiting its formation reactions. Small particles decrease carbon deposition rate [6], however, are more susceptible to sintering and oxidation. Variation of the method of incorporation of the active phase in a catalyst could result in different physicochemical properties, allowing a low carbon amounts and increasing the stability of Ni catalysts [7,8]. In addition, the characteristics of the precursor species of the active phase often affect the catalyst surface properties and its catalytic behavior. The choice of a precursor is a very important step in catalyst preparation. Aqueous solutions containig chelating agents in the wet impregnation method has been reported as a strategy to promote smaller active phase particles [9]. Van Dillen et al. [9] have pointed out that the use of aqueous solutions of chelating agents in the conventional wet impregnation method is very attractive, since it retains the simplicity of the technique and allows to obtain uniform distributions of the active phase and, in general, greater dispersions. A characteristic of these solutions is that, during the solvent remotion, the viscosity of metal complex solutions increases substantially due to a gelling process, affecting the drying stage, inhibiting the redistribution of surface species and favoring the formation of poorly crystallized

compounds with high dispersion. In literature, the use of chelating agent has been reported mainly in the synthesis of hydrodesulfurization catalysts [10-12], catalysts for Fischer-Tropsch synthesis [13,14] and recently, for reforming catalysts [15-17].

The incorporation of chelating agents into a transition metal solution generates metal complexes that are charged. In the catalysts preparation by using these impregnation solutions is necessary take into account factors such as: chelating agent/metal ratio, pH of impregntation solution and the point of zero charge (PZC) of support [18]. Some published works on ESR have reported important improvements in catalytic properties by using citric acid (CA) [19,20]. Nitrilotriacetic acid, NTA, and CA are chelating agents with the same amount of carbon atoms. NTA have carboxylates and nitrogen groups, while CA has carboxylate groups and a hydroxyl group. The donor capacity of a chelating agent is given by the amount of binding sites presents in its structure, both functional groups and coordination sites, as well as the pair of free electrons of the nitrogen atom in NTA or oxygen atom in CA. The greater the electron-giving capacity of a chelating agent, the greater the bond strength with the central ion [21] and consequently more stable will be the complex formed. NTA and CA acids have the same amount of functional groups and coordination sites. However, NTA forms complexes more stable with nickel and cerium than CA [22], then it is interesting to compare the behavior of both acids.

On the other hand, in the literature has been reported the modification of acid/base properties of supports by addition of modifiers such as alkaline metals (Na, K), alkaline earth metals (Mg, Ca) or the addition of rare earth oxides (Ce, La, Pr) [3,8,23]. CeO_2 has been used as a support or promoter because its particular properties of oxygen storage and release that to allow carbon deposits to be gasified and to the presence of the Ce^{3+}/Ce^{4+} couple [24-26]. Elmhamdi et al. have also pointed out the importance of having CeO_2 at a nanometric level to enhance its properties [27]. In previous work, the decrease of Ni and CeO_2 crystaline sizes on $Ni/MgAl_2O_4$-CeO_2 catalysts due to the use of chelating agents has been reported [28]. The system prepared in the presence of nitrilotriacetic acid (NTA), with a molar ratio of NTA/Ni=1 showed a good performance in ESR, obtaining high selectivity to H_2 and high resistance to carbon deposition [28]. In addition, the effect of EDTA/Ni molar ratio was examined in the synthesis of Ni catalysts [29]. The capacity of EDTA to form stable complexes with nickel and cerium promotes a better interaction between Ni and CeO_2 and decreses the size of NiO and CeO_2. A catalyst prepared using the stoichiometric ratio for the complete complexation of nickel (EDTA/Ni molar ratio=1) showed the best performance in the ethanol steam reforming reaction under mild operation conditions and presented small crystallite size, and higher Ce^{3+}/Ce^{4+} and Ce/Ni^0 ratios.

In this article, the use of different amount of NTA or CA as chelating agent in the synthesis of supported-Ni catalysts and their influence in ESR reaction are discussed.

2. Experimental

2.1. Catalyst Preparation

Nickel catalyst were synthetized following the procedure reported in [28]. Briefly, $MgAl_2O_4$ was prepared using citrate method and it was modified with CeO_2 (5 wt.%, nominal loading) by wet impregnation with an aqueous solution of $Ce(NO_3)_3.6H_2O$ (Aldrich, 99%). Nickel (8wt.%, nominal loading) was incorporated over the modified support, $MgAl_2O_4$-CeO_2 (in its dried form), using aqueous solution of $Ni(NO_3)_2 \cdot 6H_2O$ (Merck, 99%) in presence of chelating agent (L), NTA (Sigma-Aldrich, 99%) or CA (Sigma-Aldrich, 99.5%), in different molar ratio L/Ni (L/Ni = 0, 0.5, 1 and 2). First, the chelating agent was dissolved using a NH_3 solution and then $Ni(NO_3)_2 \cdot 6H_2O$ solution was added. The pH of these impregnation solutions were adjusted at a pH between 6-7 (lower than the PZC of $MgAl_2O_4$-CeO_2). These solutions were aged under stirring at room temperature for 2 h. Then, 1 g of the $MgAl_2O_4$-CeO_2 was added and stirred for 1 h. The resulting suspensions were carried to an ultrasound bath at room temperature for 10 min and then the solvent was slowly removed under vacuum at 80 °C for 1 h. The dried samples were calcined in static air from room temperature to 650 °C at 10 °C min^{-1}. The catalysts were labeled as NiL(x), where x correspond to the molar ratio L/Ni, being L= NTA or CA. NiL(0) corresponds to the nickel catalyst free of chelating agent.

2.2. Characterization of catalysts

Chemical composition. The solid samples were brought into solution by an alkali fusion with $KHSO_4$ and subsequent dissolution with aqueous HCl. Ni chemical composition was measured by atomic absorption spectroscopy using Varian AA 50 equipment. Cerium chemical composition was determined by inductively coupled plasma-atomic emission spectroscopy (ICP). A sequential ICP spectrometer Baird ICP 2070 (BEDFORD) with a Czerny Turner monochromator (1m optical path) was employed.

Adsortion-desorption N_2 isotherms. The specific surface area was determined by the BET method from the adsorption-desorption isotherms of N_2 at the boiling temperature of liquid nitrogen (-195.8 °C), using a Micromeritics Gemini 5 equipment. Previously, samples were degassed at 250 °C for 16 h in N_2 flow. From the desorption branch, pore volume and pore distribution values were obtained using the BJH model (Barreto, Joyner and Halenda) suitable for mesoporosity determination.

Temperature programmed reduction (TPR). The redox properties of the samples were examined using conventional equipment. Before to the TPR experiments, the samples were treated in O_2 flow (17%)/He (36 mL min^{-1}) at 300 °C by 1 h and then in He flow (30 mL min^{-1}) by 30 min. After cooling in He samples were reduced in flow of H_2(5 vol.%)/N_2 (50 mL min^{-1}) from ambient temperature up to 950 °C at 10 °C min^{-1}, keeping this temperature for 1 h.

Fourier Transformed Infrared spectroscopy (FTIR). The samples were analyzed by infrared spectroscopy using an FTIR Nicolet Protégé-460 spectrophotometer, in a range of 4000-250 cm^{-1} with a resolution of 4 cm^{-1} and 64 scans. The samples were mixed with KBr at approximately 1 wt.%, crushing the mixture into an agate mortar. Then, the mixture was compressed at a pressure of 300 Kg m^{-2} and room temperature.

UV-Vis and UV-Vis-NIR spectroscopy. The UV-Vis spectra of the different impregnation solutions were obtained using an Agilent 8454 spectrophotometer with diode network detector using the 8453 UV Visible

ChemStation Rev.A.10.01 software, associated with the instrument. Catalytic samples were packed using $BaSO_4$ as blank and placed on the integrative sphere, ISR-3100. The Shimadzu UV-3600 was operated in diffuse reflectance mode in the UV-Vis-NIR (DR UV-Vis-NIR) range. The spectra for all samples were taken between 2500-200 cm^{-1} with a slit of 5 nm.

*X-ray diffraction (XRD).*The diffraction patterns of the samples were obtained in a RIGAKU (ULTIMA IV) diffractometer operated at 30 kV and 20 mA using CuKα radiation (λ=1.5418 Å) with Ni filter and horizontal goniometric. The data were acquired at 3º min^{-1}, for values of 2θ between 10 and 70°. The powder samples were placed without any prior treatment in a flat glass sample holder. The identification of the crystalline phases was performed using reference patterns (JCPDS files of the ICDD). To study the crystallite size, the patterns were recorded in a step mode (2θ=10-90°; step = 0.02° and counting time: 5 s) and refined by the Rietveld method using the Fullprof program [30,31]. For this purpose, the identified phases were considered with the following structural models: $MgAl_2O_4$ (cubic, $Fd\bar{3}m$), CeO_2 (cubic, $Fm\bar{3}m$), NiO (cubic, $Fm\bar{3}m$) and Ni (cubic, $Fm\bar{3}m$). The shape of the peaks was modeled using the Thompson-Cox-Hastings pseudo-Voigt function [32]. In some samples the crystallite size was obtained by applying the Scherrer equation [33]:

$$\beta = \frac{K\lambda}{d\ cos\theta}$$

β is the width of the peak corresponds to a given value of 2θ, λ corresponds to the wavelength of the X-rays, K is a constant that is a function of the crystalline shape, but is generally taken equal to 0.9 for spherical particles and d corresponds to the crystallite size. The width of the peak in XRD gives an average value of the crystallite size.

X-ray photoelectron spectroscopy (XPS). XPS analysis was performed on a SPECS Multitechnical equipment equipped with an Mg/Al dual X-ray source and a PHOIBOS 150 hemiespheric analyzer in Fixed Analyzer Transmission (FAT) mode. The spectra were obtained with a pass-through energy of 30 eV and Al anode operated at 200 W. The pressure in the analysis chamber during the measurement was less than 2.10^{-8} mbar. To reduce the load effect on the samples, a "flood gun" electron cannon was used. Before acquisition of the spectra, samples were subjected to an in-situ reduction in H_2/Ar flow for 10 min at 400 °C, and then evacuated to a pressure less than 2.8 x 10^{-7} mbar for at least two hours before readings.

High resolution transmision electron microscopy (HRTEM). A TECNAI F20 FEI equipment with field emission source at 200 kV and a resolution of 0.19 nm was used for transmission electron microscopy. The samples were deposited in lacey-carbon Cu grids.

Thermal gravimetric analyses (TGA). The decomposition of the precursors of dried catalytic systems was performed in oxidizing atmosphere in a TGA 51 Shimadzu unit, with an air flow of 50 mL min^{-1} from ambient temperature up to 800 °C at 5 ° min^{-1}. The amount of carbon deposited on catalysts after the ESR reaction was studied in oxidizing atmosphere under an air flow of 50 mL min^{-1}, from ambient temperature to 900 °C with a heating rate of 10 °C min^{-1}. The samples were placed in a platinum capsule. The percentage of carbon deposited during the reaction for catalysts was calculated using the following equation:

$$\%C = \frac{(W_{initial} - W_{final}) * 100}{W_{final}}$$

($W_{initial}$ - W_{final}) is the amount of carbon on the catalyst and W_{final} is the final weight of sample after TGA analysis.

Raman spectroscopy. Renishaw's inVia Qontor Raman microscope equipment was used. The spectra were taken with the visible laser of 532 nm with 15 accumulations (3 s), in the range between 600-1800 cm^{-1}.

Scanning electron microscopy and energy dispersive X-ray spectroscopy (SEM-EDAX). For qualitative determination of the local composition and texture of catalyst surfaces, a scanning electron microscope, LEO 1450 VP equipped with an EDAX Genesis 2000 microchannelizer with Si (Li) detector, was used. The samples were metalized with gold to prevent them from loading.

2.3. Catalytic experiments

Catalytic tests of the ESR reaction were carried out at 650 °C, at atmospheric pressure, in a quartz tubular reactor (4 mm internal diameter), for 7 h. A previous *in-situ* reduction procedure was performed with a flow of H_2(5%) in N_2 for 45 min at 650 °C. The catalyst weight was 0.05 g with a particle size range between 0.3-0.4 mm (35-50 mesh) without dilution. The reactor feed consisted of liquid mixture of ethanol and water (0.15 mL min^{-1}), which was evaporated at 130 °C in a He flow free of O_2. The water/ethanol molar ratio was equal to 4.85, with a composition of 9.4 % ethanol (y_{C2H5OH}) in the feed at an ethanol flow of 1.0210^{-3} mol min^{-1}. The space-time was 0.018 g_{cat} h/g_{C2H5OH} (49 g_{cat} min/mol_{C2H5OH}). This reduced space-time allows early detection of any deactivation effect [5].

Reagents and reaction products were analyzed online by two gas chromatographs. H_2, CH_4 and CO_2 were determined with TCD using N_2 as internal standard; while CO (previous passage by a methanator), C_2H_4O, C_2H_4 and C_2H_5OH without reacting and other compounds containing carbon, with the FID.

Ethanol conversión was calculated as:

$$X_{\mathrm{C2H5OH}} = \frac{F^{in}_{\mathrm{C2H5OH}} - F^{out}_{\mathrm{C2H5OH}}}{F^{in}_{\mathrm{C2H5OH}}} * 100$$

F_{C2H5OH} is the molar ethanol flow; *in* and *out* corresponds to inlet and outlet flow of the reactor.

Selectivity to carbon products was calculated as:

$$S_i = \frac{ni\ F_i^{out}}{2\left(F^{in}_{\mathrm{C2H5OH}} - F^{out}_{\mathrm{C2H5OH}}\right)} * 100$$

F_i^{out} is the outlet flow of each hydrocarbon and *ni* is the number of carbon atoms in each product *i.*

Hydrogen yield was calculated as:

$$Y_{H2} = \frac{F_{H2}^{out}}{F_{\mathrm{C2H5OH}}^{in}}$$

F_{H2}^{out} is the outlet flow of hydrogen of the reactor.

3. Results and discussion

3.1. Impregnation solutions

Thermodynamic speciation diagrams of nickel were obtained using Medusa Software [34]. Table 1 shows the predominant nickel species in impregnation solutions used in the synthesis of catalysts. The synthesis of catalysts was made by impregnation of support using a solution with a pH below to the PZC of the support (PZC=9.6 [28]) to ensure a strong interaction between complex with negative charge and the surface of support with a positive charge. At pH of impregnation solution, the thermodynamic diagrams predict the formation of different nickel species at 25 °C. Only one complex species in solution, $[Ni(NTA)(H_2O)_2]^-$ and $[Ni(CA)_2]^{4-}$, was predicted by employing a L/Ni ratio leading to the most stable complex formation (NTA/Ni=1 and CA/Ni=2). Different nickel species in solution were predicted for the other L/Ni ratios and they could promote different interactions with the support affecting its catalytic properties.

Table 1. Nickel species at pH of impregnation solutions.

System	pH	I*	Complex in solution
Solution L-Ni(0)	5.9	0.4	$[Ni(H_2O)_6]^{2+}$
Solution NTA-Ni(0.5)	6.6	1.3	$[Ni(NTA)(H_2O)_2]^-$; $[Ni(H_2O)_6]^{2+}$; $[Ni(NH_3)(H_2O)_5]^{2+}$
Solution NTA-Ni(1)	6.7	1.9	$[Ni(NTA)(H_2O)_2]^-$
Solution NTA-Ni(2)	6.6	2.3	$[Ni(NTA)(H_2O)_2]^-$; $[Ni(NTA)_2]^{4-}$
Solution CA-Ni(0.5)	6.5	1.6	$[Ni(CA)(H_2O)_2]^-$; $[Ni(CA)_2]^{4-}$; $[Ni(NH_3)(H_2O)_5]^{2+}$
Solution CA-Ni(1)	6.5	1.6	$[Ni(CA)_2]^{4-}$; $[Ni(CA)(H_2O)_2]^-$; $[Ni(NH_3)(H_2O)_5]^{2+}$
Solution CA-Ni(2)	6.6	2.4	$[Ni(CA)_2]^{4-}$

*I=Ionic strength

UV-vis spectra of the impregnation solutions allow to identify the nickel coordination in the solution, Figure 1A. The figure shows the UV-Vis spectra of the impregnation solution containing NTA and CA with different

L/Ni molar ratio. In the UV zone is observed at 300 nm the π-π* transition of the NO_3^-. The visible zone of the spectra shows the d-d transition of Ni^{2+} in an octahedral environment (Table 2 [35, 36]), allowed transitions: λ_1: $^3A_{2g}$ (F) → $^3T_{1g}$ (P); λ_2: $^3A_{2g}$ (F) → $^3T_{1g}$ (F); λ_3: $^3A_{2g}$ (F) → $^3T_{2g}$ (F); and forbidden spin transition: λ_{fs}: $^3A_{2g}$ (F) → ^1E_g (D). The blue shift of the nickel bands using NTA or CA with different L/Ni ratios reveals the complex formation under the experimental synthesis conditions. The chelating agent, NTA or CA, produces a slight blue shift, indicating the complex formation by water substitution in $[Ni(H_2O)_6]^{2+}$ [37].

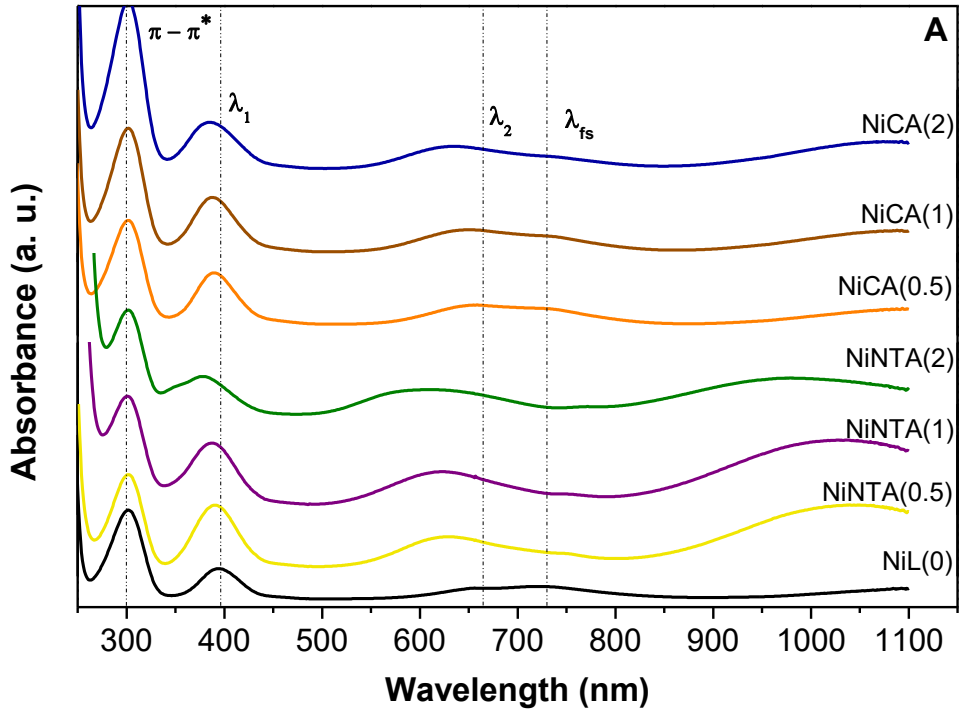

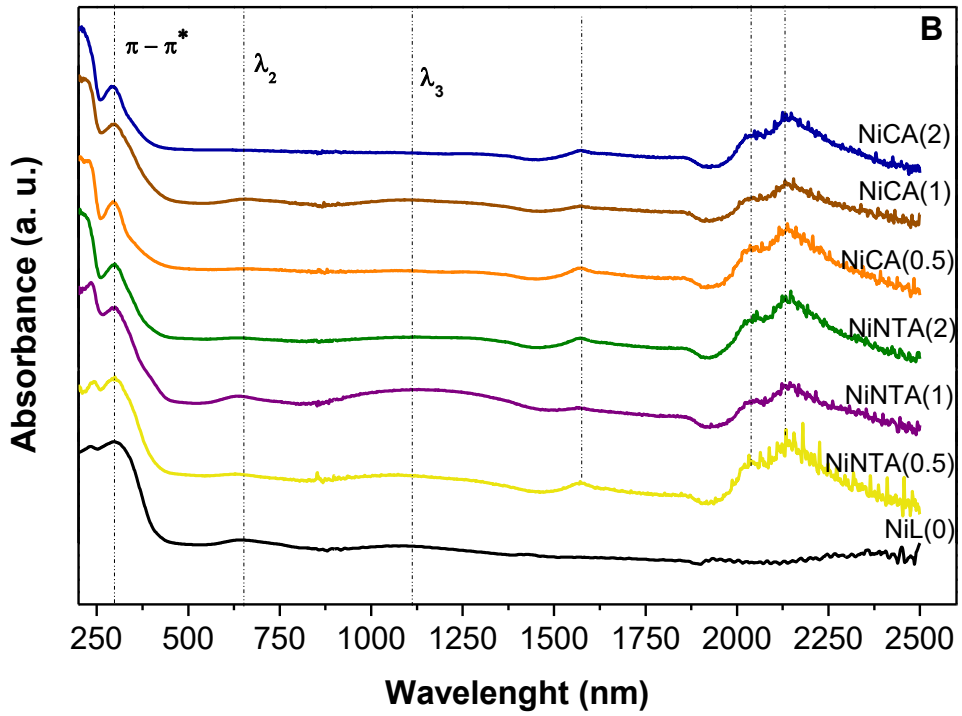

Figure 1. UV-Vis spectra of impregnation solutions (A) and DR UV-Vis-NIR spectra of dried catalysts (B).

3.2. Dried systems

The nickel coordination on the surface of dried catalysts was studied by DR UV-Vis-NIR spectroscopy. From a comparation between impregnation solution spectra and dried catalysts spectra is possible to identify if the complex in solution is maintained in the dried system. Figure 1B shows the DR UV-Vis-NIR spectra of dried systems. Between 200-300 nm is observed a band associated with $O^{2-} \rightarrow Ce^{4+}$ transition and/or 4f→ 5d of Ce^{3+} transition [38] or associated with charge transference between $O^{2-} \rightarrow Ni^{2+}$ [39]. In all spectra a band at 300 nm associated with the π-π* transition of NO_3^- without coordination is observed, interacting only by physical adsorption with he support [35,40]. Table 2 shows the transitions in dried systems compared to impregnation solutions. For all dried systems, in the Vis-NIR zone, is observed two bands, λ_2 and λ_3, between 500 and 1500 nm, while the λ_1 transition could be overlap with band at 300 nm. In the NiL(0) dried sample is noted a slight blue shift respect to the bands in its impregnation solution. This indicates that the nickel aquo complex, $[Ni(H_2O)_6]^{2+}$, is interacting as such with the support. The positions of the bands in the NiNTA(x>0) dried samples have experimented a slight red shift respect to bands of impregnation solutions. The same occurs in the NiCA(0.5) and NiCA(1) dried samples. Unexpectedly, the Ni^{2+} bands are low intensity in the NiCA(2) system. The red shift or towards higher wavelength values indicate that the nickel complex on the surface is a lower strength field. This red shift is related to a bonding weakening among the chelating and Ni^{2+} by formation of hydrogen bonding between OH groups of the support and the oxygen atoms of chelating agent. During drying step the chelated metal precursor forms a gel-like phase and this gel would sufficiently interact with the support

[9]. Ortega-Domínguez et al. [41] have informed similar results using a Ni-EDTA impregnation solution over SBA-15. Koizumi et al. [42] have reported the same interaction between NTA and Co^{2+} in the solution and claimed that it was maintained on the dried surface of Co catalysts synthesized with NTA. NIR zone, between 800-2500 nm, shows a band around to 1570 nm corresponds to first overtone of ν(NH) vibration [43]. Between 1500 and 2500 nm vibrations related to chelating structures are observed (they are not present in the NiL(0) dried spectrum). NiL(0) dried sample only shows a band at 1425 nm that corresponds to first overtone of OH neutral specie. In the NiNTA(x>0) or NiCA(x>0) are not observed major differences with the increase of chelating agent, indicating that the nickel complex on the surface of the dried systems could have the same nature.

Table 2. Electronic transitions of Ni^{2+} in the NiNTA(x) and NiCA(x) systems.

Sample	**λ_1 (nm)**	**λ_2 (nm)**	**λ_{fs} (nm)**	**λ_3 (nm)**
NiL(0)	n.d.	645	n.d.	1080
Solution L-Ni(0)	394	655	728	> 1100
NiNTA(0.5)	n.d.	635	n.d.	1074
Solution NTA-Ni(0.5)	390	628	748	1040
NiNTA(1)	n.d.	635	n.d.	1139
Solution NTA-Ni(1)	387	620	748	1030
NiNTA(2)	n.d	637	n.d.	1040
Solution NTA-Ni(2)	378	600	--	985
NiCA(0.5)	n.d.	667	n.d.	1092
Solution CA-Ni(0.5)	390	650	733	> 1100
NiCA(1)	n.d.	659	n.d.	~1100
Solution CA-Ni(1)	387	645	735	> 1100
NiCA(2)	n.d.	n.d.	n.d.	n.d.
Solution CA-Ni(2)	385	630	735	> 1100
Reference $[Ni(H_2O)_6]^{2+}$	395	650	741	1175

n.d= not detected

In order to identify the species on the surface in the dried systems, the samples were examined by FT-IR analyses (Figure 2). All the systems prepared with NTA or CA shows, between 2600 and 3700 cm^{-1}, a band associated with OH group vibrations (3470 cm^{-1}) and bands corresponded to symmetric and asymmetric stretching of CH_2 (3140-2800 cm^{-1}) [44]. In 1630 cm^{-1} appears the band of H_2O deformation (δH_2O) [45]. The characteristic sharp bands of nitrate are observed in agreement with the NO_3^- π-π^* transition assigned in UV-Vis spectroscopy . In particular, the transitions of nitrate ion at 826 and 1765 cm^{-1} are observed in all the dried samples and the transitions at 1393 and 1630 cm^{-1} are less notorious in the systems prepared with chelating

agents. The bands detected between 1700-1200 cm^{-1} correspond to contribution of carboxylates group bonded to a metal and the presence of nitrate ion without coordination [46]. Furthermore, it is not observed an additional band to values up than 1630 cm^{-1} indicating the absence of carboxylates without coordination [47,48]. This indicated that the major contribution for all the dried systems prepared with NTA or CA corresponds to the symmetric stretching of COO^- (ν_s) and asymmetric stretching of COO^- (ν_{as}) [49] and it indicates that the metal is coordinated by carboxylate groups belonging to chelating agents regardless of the molar L/Ni ratio used.

Infrared spectra of calcined systems (Figure S1) show symmetric and asymmetric bands of COO^- groups. This carbonaceous species corresponds to wastes of the synthesis of the support. They remains after the combustion of citric acid used in $MgAl_2O_4$ preparation at 650 °C for 3 h [29]. It is not observed differences in the spectra of calcined samples when NTA or CA is used in the impregnation solutions. This indicate that the vibrational nature of oxide species is similar in all catalysts independently of chelating agent and its used quantity.

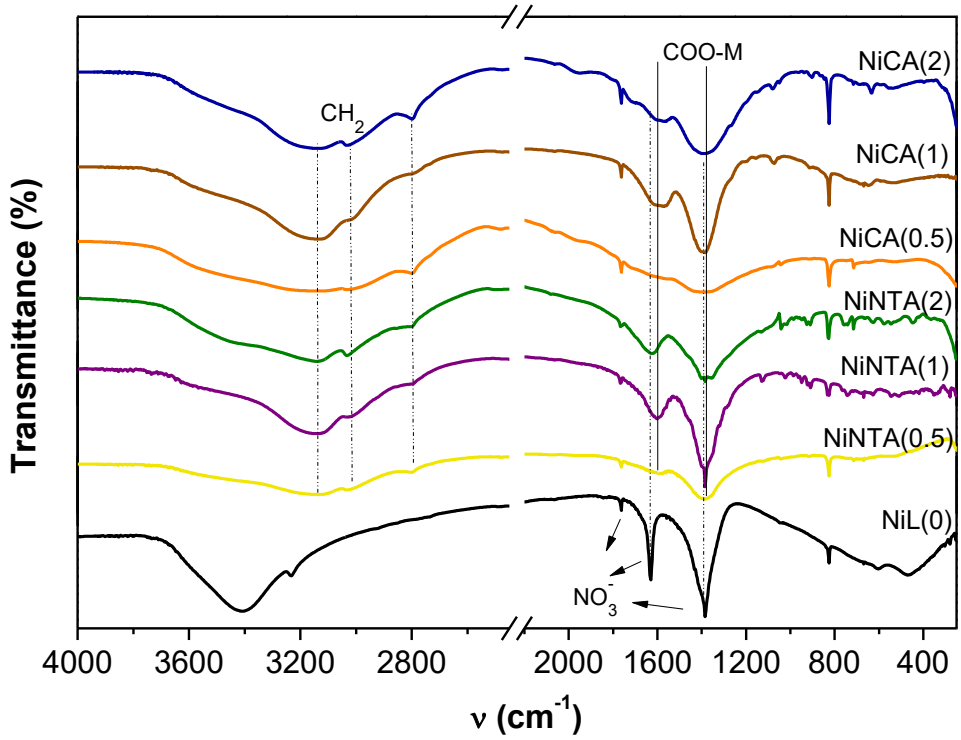

Figure 2. Infrared spectra of dried catalysts.

Thermal decomposition of precursor was studied under an oxidant atmosphere. Figure S2 shows the thermograms and dweight/dt vs. temperature of dried catalysts where different weight loss events are observed. The theoretical weight losses considering that precursor decomposition leads to NiO are shown in Table S1. The experimental values are lower than the theorical ones, except for the NiCA(0.5) sample. Similar results were observed with catalysts prepared with EDTA [29], suggesting that the decomposition began in the dried step. In the sample free of chelating agent, NiL (0), the weight loss up to 100 ° C could be assigned to the elimination of physisorbed water, and that at 300 ° C corresponds to the combustion of the precursor to produce

NiO [50]. For the NiNTA(x>0) systems are observed differences in the number of weight loss events associated to decomposition of different precursor species. NiNTA(0.5) shows significant weight loss from 230 °C to constant weight at 400 °C. The maximum decomposition temperature at 245 °C is associated to the decomposition of the nickel aquocomplex and the complex with NTA. The maximum decomposition temperatures are detected at 231, 294 and 360 °C for NiNTA(1), while two weight loss events are observed at 245 °C and around 375 °C for NiNTA(2). The latter event is related with to decomposition of free NTA. In the NiNTA(x>0) systems are not possible dismiss the Ce-NTA complex formation. NiCA(0.5) only shows a weight loss at 245 °C, while in NiCA(1) are observed three weight loss events at 233, 278 and 358 °C. The main weight loss is showed at 243 °C and a smaller one at 393 °C for NiCA(2). The presence of a weak peak between 300 and 500 °C is only observed in NiCA(1) sample. Probably the interaction between CA and Ce is negligible, its stability constant is lower in comparison with NTA. Wang et al. [44] have studied the decomposition in air of Na_2[Ni(CA)]. These authors have identified two combustion events: a weight loss between 30-340 °C attributed to coordinated water removal and CO_2 release, and the latter in the range of 340-520 °C to the combustion of the organic component. They did not observe mass changes at temperatures below 300 °C, and considered that some of the H_2O had been incorporated into the structure of the complex like [Ni(CA)$(H_2O)_3$].

3.3. Fresh and reduced catalysts

Table 3 shows the values of chemical composition obtained for the catalysts. Nickel and cerium content were lower than the nominal values probably due to the precursor salts are easy to hydrate. For NiNTA(2) and NiCA(2) the Ni values are higher and this fact will contribute to its performance catalytic. N_2 adsorption-desorption isotherms are shown in Figure S3. The isotherms are IV type with H2 hysteresis for all the catalysts in this work, this is typic for mesoporous solids with cylindric porous or aggregates or agglomerates of spherical particles with non-uniform size and shape [51]. The S_{BET} values are presented in Table 3. A decrease in all the catalysts respect to the support, $MgAl_2O_4$-CeO_2, S_{BET} = 102 g/m^2 is observed. This decrease could be related with the thermal treatment after the impregnation step or the porous blockage by NiO phase impregnated [52]. The S_{BET} for the catalysts is not affect for the nature of the chelating agent and for the molar ratio L/Ni. Porous volume distribution (Figure S3) is similar for all the catalysts independently of precursor used in the synthesis. The catalysts have larger porous respect to $MgAl_2O_4$-CeO_2, with a high contribution of porous between 2 and 8 nm and an increase in the porous size associated with decomposition of precursor during the calcination step [53].

Table 3. Some properties of catalysts synthesized with NTA and CA.

Sample	**Ni wt.%**	**CeO_2 wt.%**	**S_{BET} (m^2/g)**	**d_{pore} (nm)**	**V_{pore} (cm^3/g)**
NiL(0)	5.7	4.4	88	4.9	0.14
NiNTA(0.5)	6.5	4.7	95	4.7	0.14

NiNTA(1)	6.3	5.4	92	5.8	0.17
NiNTA(2)	8.2	5.6	99	5.0	0.15
NiCA(0.5)	6.8	5.2	91	5.0	0.13
NiCA(1)	5.0	4.5	80	5.4	0.14
NiCA(2)	9.0	4.5	94	4.9	0.15
$MgAl_2O_4$-CeO_2	--	n.d.	102	4.4	0.08

n.d.= not determined

X-ray patterns of fresh catalysts are shown in Figure 3. $MgAl_2O_4$, CeO_2 and NiO phases are observed in all the catalysts. Table 4 shows the crystallite size of NiO and CeO_2 phases determined by Scherrer equation (between brackets) using the peaks in $2\theta = 43°$ and 28°, respectively. The broadening of the peaks in $2\theta = 43°$ of the NiO phase shows that the use of NTA promotes the formation of smaller NiO crystallites regardless of the amount of used NTA respect to the NiL(0). In addition, NiNTA(1) and NiNTA(2) samples show a broadening of peak in $2\theta = 28°$ corresponding to CeO_2, this effect is less notorious in NiNTA(0.5) system. $MgAl_2O_4$-CeO_2 support is used without calcination and it has verified that a CeO_2 dissolution occurs during impregnation step [29]. Similar results were reported by Santolalla-Vargas et al. [54] in the preparation of W catalysts. The authors indicated a redispersion of W on the surface when the impregnation solution containing CyDTA as a chelating agent is mixed with dried γ-Al_2O_3 support promoting the formation of different W species. 0.5 NTA mol per Ni mol would promote the complexation only of Ni^{2+} ion while a higher amount of NTA (NTA:Ni = 1 or 2) could also afford an interaction with Ce^{3+} in the solution. The redispersion of ceria on the NiNTA(1) and NiNTA(2) samples allows its redeposition as amorphous particles or smaller crystallites. CeO_2 crystallite size reduction induces changes in its properties allowing an effective interaction with nickel phases on the surface. Moreover, this interaction between Ni and Ce promoted by the use of chelating agent has started in the impregnation solution [27,55]. The use of the CA also promotes the NiO crystallite size decrease and a slight effect in those of CeO_2, Table 4. This allows to infer that the CA rather interacts with Ni^{2+} and not with Ce^{3+}, in agreement with that observed by TG analysis (Figure S2).

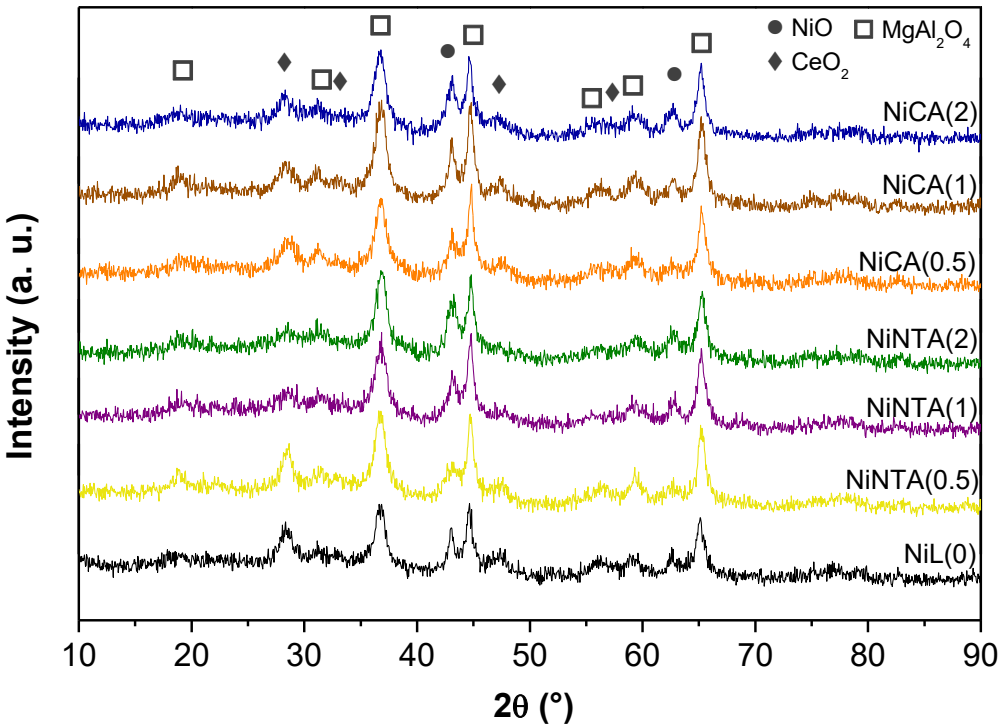

Figure 3. XRD patterns of fresh catalysts.

X-ray diffractograms of reduced catalysts are shown in Figure 4. $MgAl_2O_4$, CeO_2, Ni and NiO phases are identified in all diffraction patterns. The crystallite sizes of the phases are shown in Table 4. The presence of NiO phase reveals that reduction during 45 min at 650 °C under H_2/N_2 flow was incomplete. The intensity of this peak in $2\theta = 43°$ is high in the NiL(0), NiNTA(2) and NiCA(1) samples related to the presence of major amount of Ni^{2+} species hard to be reduced. Between 50 and 53° is observed a Ni^0 peak. Ni^0 crystallite size of catalysts prepared with NTA follows the order: NiNTA(2) ~ NiNTA(0.5) < NiL(0) ~ NiNTA(1). The CeO_2 crystallite size follows the order: NiNTA(2) ~ NiNTA(1) < NiL(0) ~ NiNTA(0.5). The use of the molar ratio NTA/Ni=2 generates smaller Ni^0 and CeO_2 crystallites. XRD of NiNTA(2) also shows a high intensity of NiO peak, probably by an excess of nickel content in this sample. The use of CA leads to smaller Ni^0 crystallite size respect to NiL(0), Table 4. In NiCA(x) systems, the Ni^0 crystallite size follows the order: NiCA(2) < NiCA(0.5) < NiCA(1) < NiL(0). The CeO_2 crystallite size follows the order: NiCA(2) < NiCA(0.5) ~ NiCA(1) < NiL(0). Li et al. [56] have reported a decrease in the size of NiO crystallite and Ni^0 in reduced Ni/SiO_2 catalysts calcinated at 500 °C and prepared in the presence of citric acid. These authors reported that the smallest crystallite size was obtained using a molar CA/Ni ratio of 1.5.

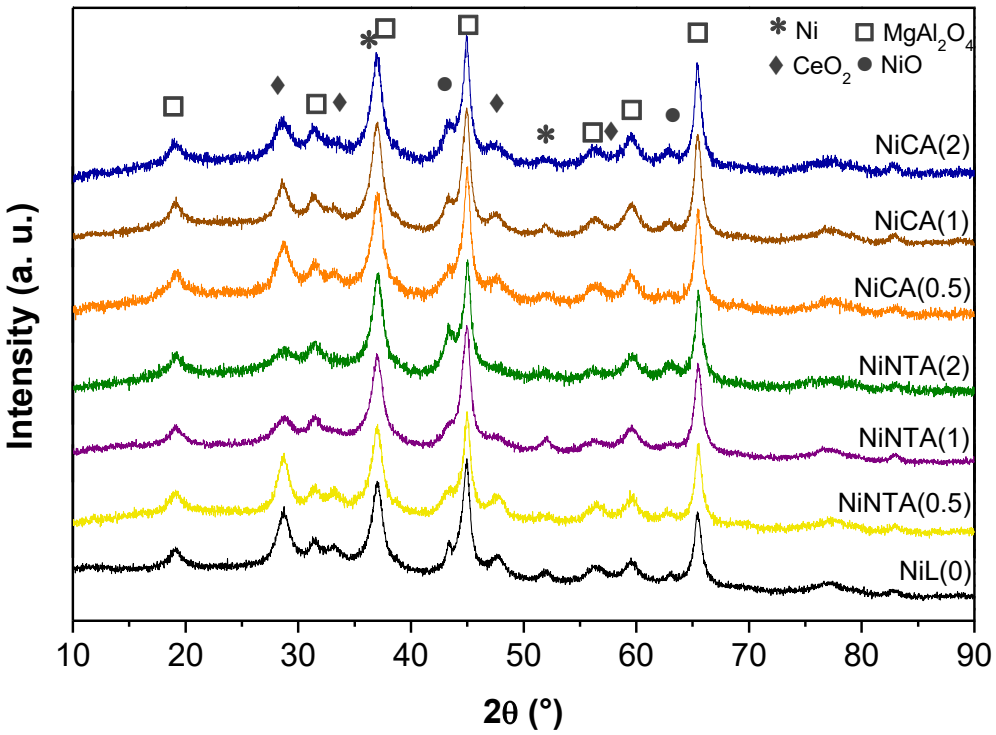

Figure 4. XRD patterns of reduced catalysts.

Table 4. Crystallite size of reduced catalysts from Rietveld refinement.

Sample	d_{Ni}^{XRD} (nm)	d_{NiO}^{XRD} (nm)*	$d_{CeO_2}^{XRD}$ (nm)*	$d_{MgAl_2O_4}^{XRD}$ (nm)
NiL(0)	4.0	13.0 (13.1)	6.0 (4.6)	5.3
NiNTA(0.5)	2.2	5.9 (7.1)	6.1 (8.9)	5.2
NiNTA(1)	4.0	6.6 (9.3)	2.7 (~ 4)	5.0
NiNTA(2)	2.0	6.6 (9.5)	1.9 (5.5)	5.0
NiCA(0.5)	2.6	4.3 (8.8)	4.4 (6.0)	4.9
NiCA(1)	3.3	7.4 (12.4)	4.4 (6.3)	4.9
NiCA(2)	2.1	6.5 (9.3)	3.2 (7.5)	4.9

* Values between brackets correspond to crystallite size of fresh catalysts obtained with Scherrer equation

The DR UV-Vis-NIR spectra of fresh catalysts, Figure 5, shows that the phase NiO is the predominant one on the catalysts and there has not been influenced by the chelating agent or the employed amount in the synthesis. This behavior is related to the stability of the support not allowing the nickel spinel formation. The most intense band at 263 nm would be associated to process of charge transference between $O^{2-} \rightarrow Ni^{2+}$ [39].

Bands around 720 and 1190 nm would correspond to Ni^{2+} transitions with an octahedral environment. The bands at 583 and 624 nm associated to the presence of $NiAl_2O_4$ phase were not detected [57,58].

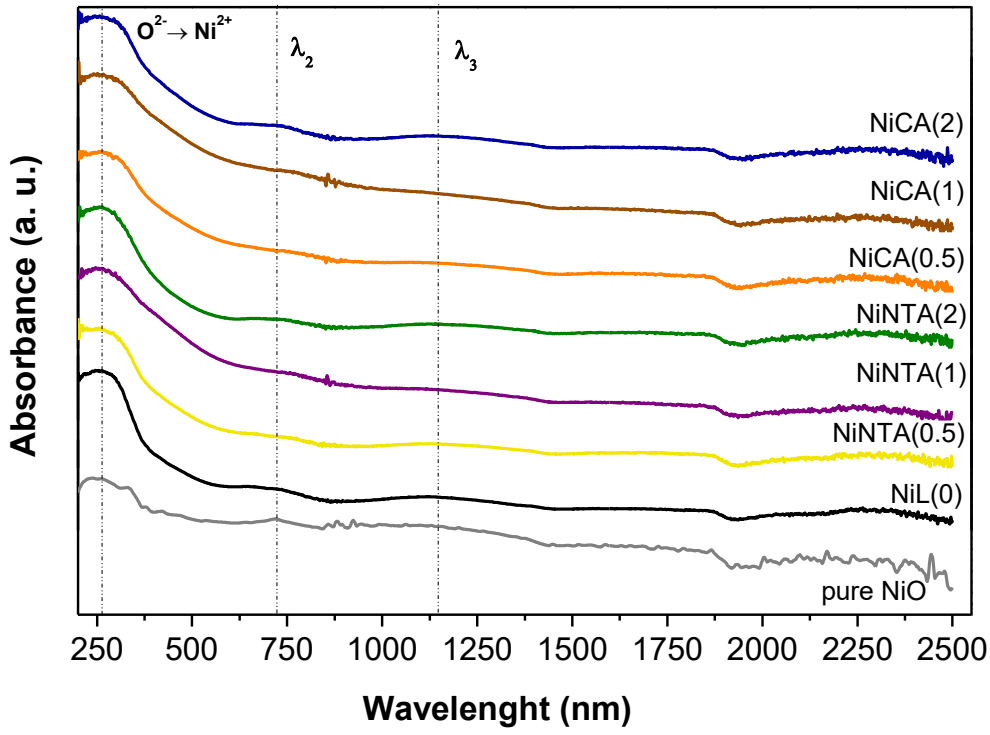

Figure 5. DR UV-Vis-NIR spectra of fresh samples.

This indicates that all the catalytic systems exhibit Ni^{2+} species with a similar coordination environment regardless the addition of NTA or CA.

From TPR profiles is possible to identify the influence of amount of chelating agent used in the synthesis on the reducibility of different species, Figure 6. All the TPR profiles are broader indicating the presence of different species. From a comparison with some results reported in literature on reducing systems containing Ni, Ce, Mg and/or Al, Table 5, the peaks in the TPR profiles could be assigned to the following species:

α species (between 200-400 °C): CeO_2 surface reduction and/or NiO amorphous species reduction;

β species (between 400-600 °C): reduction of Ni^{2+} species interacting with CeO_2 and/or Ni^{2+} species slightly interacting with $MgAl_2O_4$;

γ species (between 600-800°C): reduction of Ni^{2+} with a high interaction with $MgAl_2O_4$;

δ species: reduction of CeO_2 bulk above 750 °C.

The *γ species* were only assigned to Ni^{+2}-$MgAl_2O_4$ interactions due to the absence of DR UV-Vis-NIR bands associated to $NiAl_2O_4$, Figure 5.

The reduction profile of NiNTA(2) is similar to NiL(0), although the γ species reduce to higher temperatures. The same is observed in NiNTA(0.5) sample. The sharp peak on the TPR profiles of systems prepared with NTA is associated with β species indicating that this chelating agent promotes an intimate contact between Ni^{2+} and CeO_2. NiNTA(1) profile suggests a major contribution of β species in comparation with the other

NTA-systems. This redox behavior was verified by performing a complementary TPR experiment up to a final temperature of 700 °C on an automatic Micromeritics AutoChem II equipment. The profile showed the same behavior, Figure S4. Also, NiCA(0.5) and NiCA(1) have a notorious presence of species with intermediate reduction temperatures between 400 and 600 °C. TPR profile of NiCA(2) is similar to NiL(0), but it is evidenced a major contribution of β species. The use of NTA or CA produces the reduction of γ species at higher temperature and promotes a major contribution of β species that reduce at a lower temperature respect to NiL(0) regardless of amount of chelating agent used.

Table 5. Reduction of Ni^{2+} and/or Ce^{4+} species in the literature.

Catalytic system	TPR conditions	Reduction events	Ref.
Hydrotalcites Ni-Mg-Al-Ce	10 °C/min 80 mL/min H_2(5 %)/N_2	The incorporation of: –Ce produces a reduction of nickel spinel at lower temperatures. –Ni^{2+} into the CeO_2 network forms a solid solution allowing reduction to lower temperatures that overlap with the less interacted Ni^{2+} reduction peaks.	[45]
Ni (10 wt.%)-Ce (2.5 wt.%))/$MgAl_2O_4$	10 °C/min H_2(10 %)/Ar	The reduction starts in the Ni-Ce/$MgAl_2O_4$ system at 200 °C. The surface reduction appears at temperatures above 350 °C with the increase of Ce. The peak at: –550 °C is attributed to Ni^{2+} species in interaction with CeO_2 –780 °C is attributed to reduction of complex NiO species that interact strongly with $MgAl_2O_4$.	[55]
Ni (7 wt.%) /CeO_2-MgO	10 °C/min 50 mL/min H_2(5 %)/Ar	The peak at: –450 °C is attributed to superficial reduction of CeO_2. –315 °C is attributed to reduction of bulk NiO.	[59]
Ni/MgO (2.5, 6.25, y 12.5 wt.%)-Al_2O_3 Ni from Ni(II)-ethylenediamine (en/Ni=2)	10 °C/min 40 mL/min H_2(5 %)/Ar	α species assigned to the reduction of bulk NiO or free NiO without direct interaction with support or species with a very weak interaction. β1 species are NiO species in a Ni-riched mixed with greater interaction than α species. β2 species attributed to NiO in a Al-riched mixed phase. γ species assigned to the Ni spinel strongly associated with the spinel structure.	[60]
Ni (1.5, 4.5, y 10 wt.%)/$MgAl_2O_4$	10 °C/min 40 mL/min H_2(10 %)/N_2	The broad peak between 300 and 400 °C is attributed to reduction of NiO. The small shoulder at high temperatures corresponds to the reduction of the aluminate phase of Ni The peak at low temperatures of large NiO particles without interaction with the support.	[61]
Hydrotalcites Ni (> 9wt.%) /Mg/Al	10 °C/min 30 mL/min H_2(5 %)/N_2	The peak around 800 °C is attributed to the reduction of NiO with strong interaction with MgO and/or Al_2O_3.	[62]
Ni/xMg-ATP x=0, 5, 10, 20 wt.% ATP: attapulgite	10 °C/min 40 mL/min H_2(10 %)/Ar	Peaks between: –300-500 °C attributed to NiO with a slight interaction with γ-Al_2O_3. –500 and 700 °C attributed to a solid nickel-aluminate solution. –700 and 900 °C attributed to NiO species with strong interaction with γ-Al_2O_3.	[63]
Ni (8 wt.%)/ $MgAl_2O_4$	30 mL/min H_2(10 %)/N_2	The broad peak at 265 °C is attributed to the reduction of NiO that interact weakly with the spinel. The peak at 710 °C to small NiO particles with strong interaction with the support.	[64]
Mixed oxides $CeNi_xO_Y$	10 °C/min 33 mL/min H_2(5 %)/Ar	The low temperature peak is attributed to a solid solution between Ni and Ce or small NiO particles.	[65]
Ni(> 9.1 wt.%)/γ-Al_2O_3	10 °C/min 40 mL/min H_2(5%)/Ar	Peaks between: –350-500 °C attributed to amorphous NiO. –500-520 °C atributed to crystal NiO. –520-700 °C atributed to $NiAl_xO_y$ (a deficient-Ni-state compound). –650-800 °C atributed to $NiAl_2O_4$.	[66]

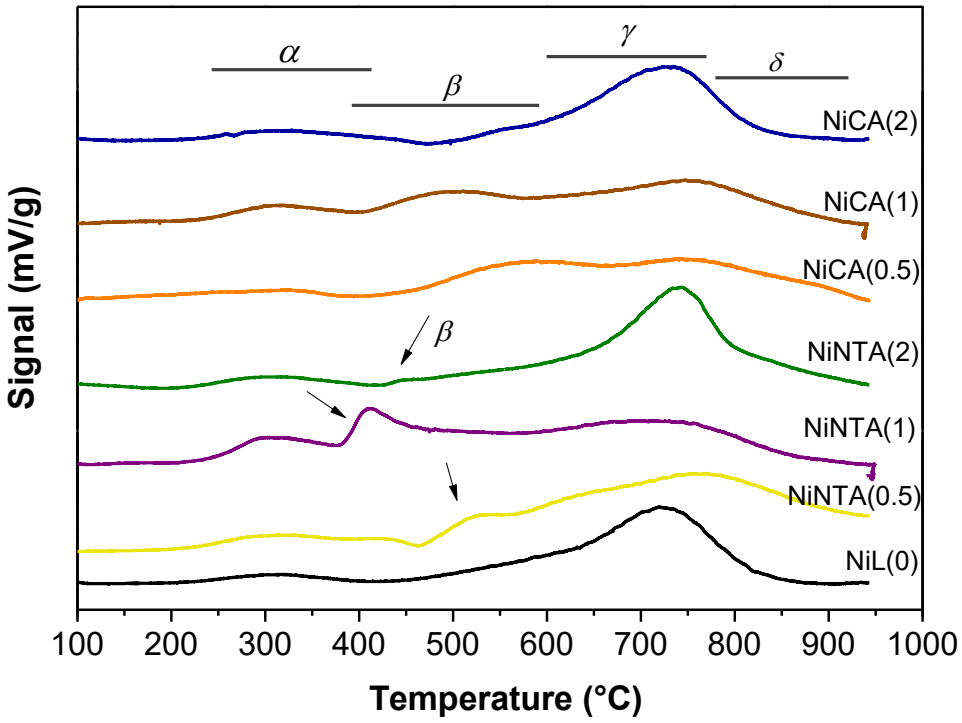

Figure 6. TPR profiles of fresh catalysts.

The influence of the amount of NTA or CA on redox properties is also studied by X-ray photoelectron spectroscopy. XPS spectra are shown in Figure 7. Fresh catalysts were reduced *ex situ* at 650 °C for 45 min in H_2(5%)/N_2 flow. Before recording XPS spectra,the samples were *in situ* reduced at 400 °C for 10 min in the pre-chamber of the equipment, in order that the contribution by Ni^0 oxidation in contact with the atmosphere can be considered negligible. The presence of Ni^{2+} in the reduced samples is related to the used reduction conditions, in line with what was observed in the XRD patterns, Figure 4. Binding energy (BE) values of the different peaks belonging to Ce 3d and Ni 2p are presented in Table 6. A slight decrease in BE values of Ni 2p is observed with the use of NTA and CA. This decrease is an indication that the addition of chelating agents increases the electronic density of Ni species. A "memory effect" of Ni species seems to be present generating distinct environments in the catalysts prepared from chelating agents [67]. It has been reported that the decrease in BE of Ni $2p_{3/2}$ is related to higher interaction between Ni and CeO_2 [58,68], which it has been also identified with the increase in the atomic ratio Ce/Ni^0 for catalysts prepared with chelating agents. In the Ce 3d region, peaks belonging to Ce^{4+} and Ce^{3+} are also observed. The presence of the Ce^{3+}/Ce^{4+} redox couple participates in carbon removal reactions and its presence increases tolerance to carbon deposition, Table 7. The values of the Ce^{3+}/Ce^{4+} ratio are higher in the NiNTA(1) and NiNTA(2) systems, being equal to 1.5, while for the sample prepared without chelating agent or with 0.5 mol of NTA, the Ce^{3+}/Ce^{4+} ratio is 0.7. This increase in the degree of surface reduction of ceria is associated with an improvement oxygen mobility [69], due to the nanometric size of the ceria and its better interaction with nickel. The higher Ce^{3+}/Ce^{4+} ratio values correspond to systems with smaller crystallite sizes of CeO_2, NiNTA(1) and NiNTA(2), Table 4. For the NiCA(1) sample, the

Ce^{3+}/Ce^{4+} ratio is 1.0. As it was already mentioned, the presence of the Ce^{3+}/Ce^{4+} redox couple participates in carbon removal reactions and its presence is key for increasing carbon deposition tolerance. The Ni^0/Ni surface ratio, considered as a measure of Ni^0 dispersion, increases with the increase of NTA in NiNTA(x) systems, Table 7. However, it do not show a clear dependence with the amount of CA. The obtained values for NiCA(x) are very similar to each other, in line with the smaller differences in crystallite sizes determined by XRD. It can be inferred that the addition of CA in the preparation produces slight changes in Ni^0 dispersion. The Ce/Ni^0 surface ratio, considered as a measure of the Ni-CeO_2 interaction, changes with the NTA/Ni molar ratio and follows the order of NiL(0) (1.26) < NiNTA(0.5) (1.70) < NiNTA(2) (1.82) < NiNTA(1) (2.80). The highest value is obtained for the NiNTA(1), catalyst what presented a TPR sharp peak related to the reduction of Ni^{2+} species interacting with CeO_2 (β species). In the same way, the Ce/Ni^0 surface ratio clearly increases by using CA in preparation, following the order of NiL(0) (1.26) < NiCA(0.5) (2.21) < NiCA(1) (2.27) < NiCA(2) (2.30).

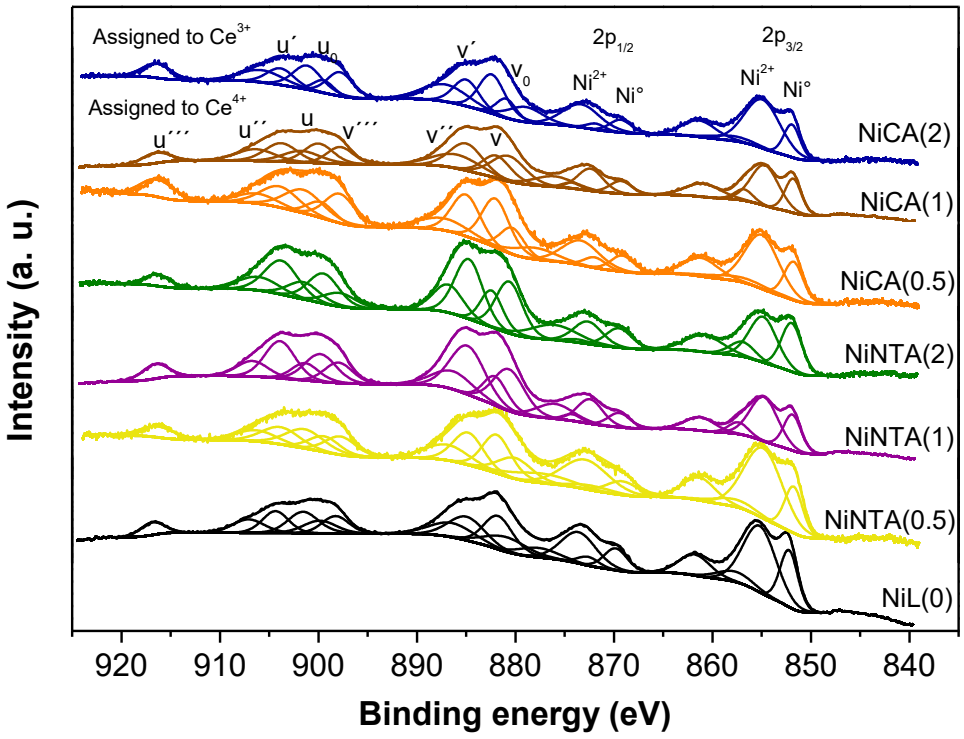

Figure 7. XPS spectra of reduced catalysts.

Table 6. Binding energy from XPS of Ni 2p and Ce 3d.

Sample	Ni $2p_{3/2}$ (eV)				Ce $3d5_{/2}$ (eV)				
	Ni^0	NiO	Ni^0_{sat}	NiO_{sat}	v_0	v´	v	v´´	v´´´
NiL(0)	852.2	855.2	857.7	861.8	880.9	884.9	881.7	886.4	898.8
NiNTA(0.5)	851.7	854.8	857.7	861.3	880.0	884.8	881.9	886.9	897.7
NiNTA(1)	851.9	854.7	857.4	861.3	880.6	884.8	882.0	886.3	898.0
NiNTA(2)	851.9	854.8	856.9	860.8	880.6	884.7	882.4	886.8	897.8

NiCA(0.5)	851.4	854.9	857.2	861.2	880.3	885.0	882.0	887.3	897.8
NiCA(1)	851.8	854.7	856.8	861.0	880.7	885.0	881.9	886.0	897.8
NiCA(2)	851.9	854.9	857.9	861.4	880.9	885.0	882.3	887.1	897.8

Table 7. Surface atomic ratio from XPS of reduced catalysts.

Sample	**Ce^{3+}/Ce^{4+}**	**Ni^0/Ni^{2+}**	**Ce/Ni^0**	**Ni^0/Ni**	**Ni/Σ***	**Ce/Σ***
NiL(0)	0.7	0.5	1.26	0.33	0.09	0.04
NiNTA(0.5)	0.7	0.3	1.70	0.25	0.12	0.05
NiNTA(1)	1.5	0.5	2.80	0.34	0.07	0.06
NiNTA(2)	1.5	0.4	1.82	0.42	0.13	0.09
NiCA(0.5)	0.6	0.4	2.21	0.29	0.09	0.06
NiCA(1)	1.0	0.5	2.27	0.32	0.06	0.04
NiCA(2)	0.4	0.3	2.30	0.24	0.11	0.06

***** Σ= Ni+Ce+Al+Mg

Representative HRTEM images of NiL(0), NiNTA(1) and NiCA(2) samples are shown in Figure 8. From these images is possible to identify different phases. These systems revealed the presence of Ni^0, NiO, CeO_2 and $MgAl_2O_4$ crystalline phases. The Fourier Transform images in different zones of the reduced catalysts show spots at 0.25-0.26 nm and 0.21 nm corresponding to (1 1 1) and to (2 0 0) crystallographic planes of NiO, respectively; spots at 0.25-0.26 nm and 0.20-0.21 nm corresponding to (3 1 1) and to (4 0 0) planes of $MgAl_2O_4$; spots at 0.26 nm and 0.30-0.33 nm corresponding to (2 0 0) and (1 1 1) planes of CeO_2 and spots at 0.19-0.21 nm of (1 1 1) plane of Ni^0. In the images CeO_2 particles with sizes less than 10 nm are observed in concordance with the crystallite size obtained from XRD, Table 4.

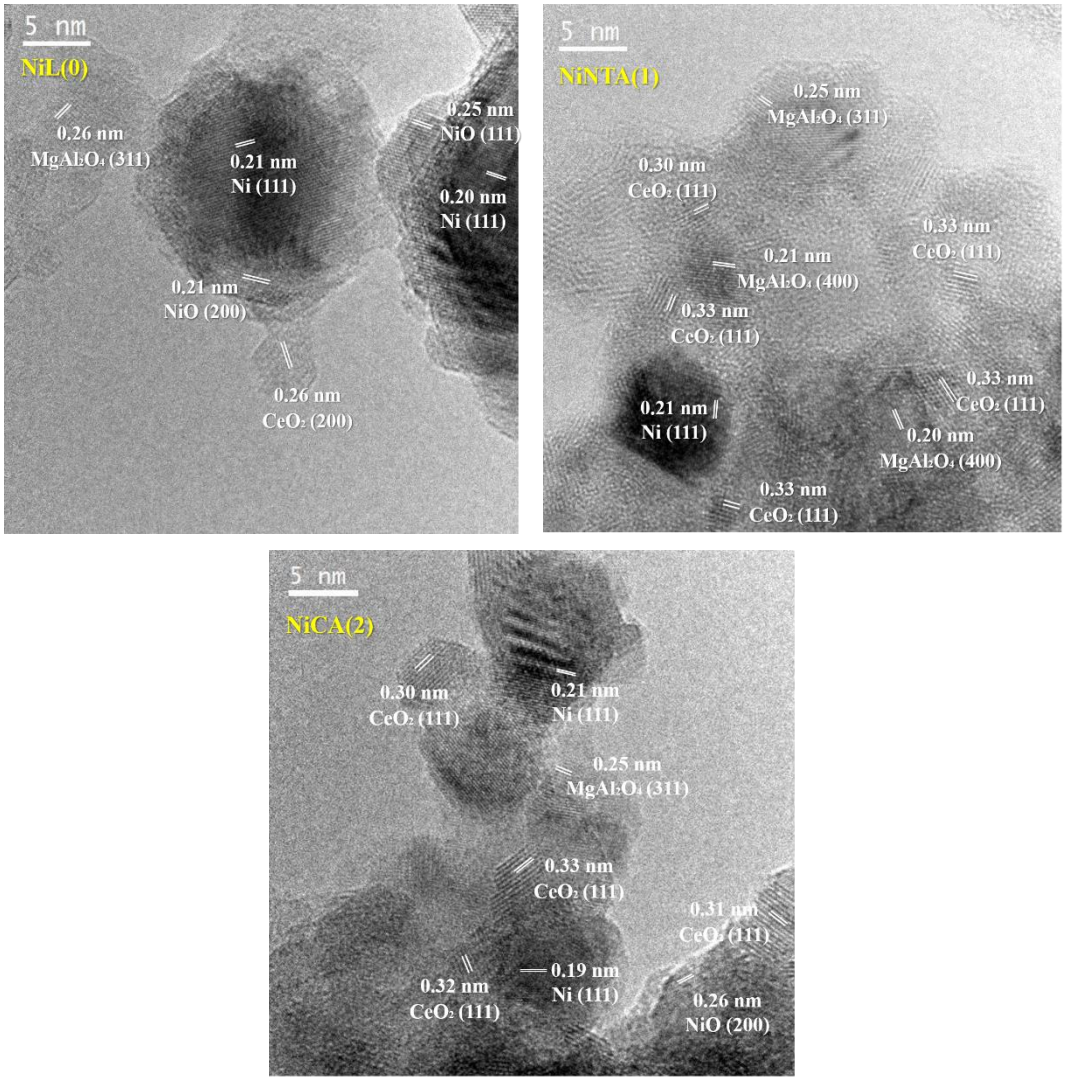

Figure 8. HRTEM images of reduced catalysts.

3.4. Ethanol steam reforming

All catalysts were tested in ethanol steam reforming reaction, Figure 9. Under the operation conditions (without bed dilution and y_{C2H5OH} = 9.2 %) used in this study, an early deactivation on the catalysts could be observed. As already mentioned, all catalysts were *in situ* reduced before an experimental run. For catalysts prepared with NTA, the ethanol conversions were higher than 80 %. In particular, the NiL(0) and NiNTA(1) catalysts were the most active, presenting average conversions of 98 and 97 %, respectively, with a slight loss of activity with operating time. The NiNTA(0.5) and NiNTA(2) samples were less active with average conversions of 86 and 91 % and a loss of activity in the order of 11 % after 7 hours in operation. The main products were H_2, CO and CO_2 and less amount of CH_4, C_2H_4O and C_2H_4. Selectivity to H_2 exceeded 60 %. Its average yield, expressed as H_2 mol per ethanol-fed mol, follows the order: NiNTA(0.5) (4.3) < NiNTA(2) (4.6) < NiL(0) (5) < NiNTA(1) (5.3 mol H_2/mol C_2H_5OH). The NiL(0) system had the lowest selectivity to CO_2,

around 43 %, while those systems prepared with NTA reached values of 50 %. CO selectivity was higher for the chelating-free system, being lower for NiNTA(0.5) and NiNTA(2) systems. For NiNTA(0) and NiNTA(1), the selectivity to minority products: CH_4, C_2H_4O and C_2H_4, were below to 6 %; while in NiNTA(0.5) and NiNTA(2), the formation of these products was higher with significant selectivities to CH_4 and to C_2H_4O. In all systems, selectivity to C_2H_4 was lower than 1.5 %. The higher selectivity of methane, of course, affects selectivity to H_2 [70]. CH_4 can be formed by the decomposition of ethanol ($C_2H_5OH \rightarrow CH_4 + CO + H_2$), and/or by the methanation of CO and CO_2 [71,72]. The catalytic results of the NiNTA(2) system are unexpected, taking into account its smaller size of the Ni^0 and CeO_2 and the high Ce^{3+}/Ce^{4+} ratio. The presence of a higher amount of Ni in its oxidized form, at the beginning of the reaction and after reduction (XRD of the reduced system, Figure 4), possibly affects the different stages in the reaction mechanism, promoting secondary reactions of formation of CH_4, C_2H_4O and C_2H_4. The best catalytic behavior was observed for the NiNTA(1) catalyst, which corresponds to the stoichiometric ratio of the most stable complex between nickel and nitrilotriacetic acid. Although, in NiNTA(1) was evidencied a slight deactivation that could be related to the type of carbon on the surface.

For all catalysts prepared with CA, the ethanol conversions were higher than 90 %. The products distribution showed slight variations. The major products were H_2, CO_2 and CO, being the selectivity to H_2 higher than 80 % in all cases. The NiCA(2) system exhibited a complete ethanol conversion during 7 h, while the other three CA-systems showed a slight decrease in activity. Its H_2 average yield follows the order: NiL(0) (5.0) < NiCA(0.5) (5.2) < NiCA(1) (5.5) < NiCA(2) (5.6 mol H_2/mol C_2H_5OH). The great differences were on the quantity of secondary products, such as CH_4, C_2H_4O and C_2H_4. The use of CA in the synthesis leads to an increase in the amount of CH_4. Thus, the NiCA(2) catalyst produced significant amounts of CH_4 as secondary product. C_2H_4O and C_2H_4 were also observed in small quantities on NiCA(0.5) and NiCA(1). For NiCA(1) a slight decay in CH_4 production with an increase in C_2H_4O was detected with time on stream, perhaps by a loss of activity in the C_2H_4O decomposition reaction [8]. From an analysis of these results, the NiCA(2) catalyst showed the best catalytic behavior. This sample presented the smallest Ni^0 crystallite size and a high Ce/Ni^0 ratio. Besides, the CA:Ni molar ratio corresponded to the stoichiometric ratio to form the most stable complex between nickel and citric acid.

A direct comparison of catalytic behavior between Ni catalysts tested in ESR is difficult due to not only catalyst features (metal percentage, support, modifiers, etc.) and synthesis conditions (different precursor salts and preparation methods) but also to significant changes in the reforming conditions (water/ethanol molar ratio, temperature, catalyst weight, degree of bed dilution, percentage of ethanol in the feed and activation conditions). Bepari et al. [45] studied a series of cerium-promoted Ni-Mg-Al hydrotalcite catalysts in the ESR. The best performance was obtained at 540 °C (operation conditions: 3.0 g_{cat}, water/ethanol molar ratio = 9 and space-time of 22.04 $kg_{cat}h$/kmol of ethanol fed) for the 5.5 % Ni and 10.5% Ce catalyst. Under this condition, about 97 % of ethanol conversion was obtained with a H_2 yield of 4.3 mol H_2/mol C_2H_5OH, also were detected CO_2, CO and CH_4 as products. Słowik et al. [19] prepared a Ni/CeO_2 catalyst using an aqueous solution of nickel nitrate with citric acid CA (Ni/CA =1), calcined at 420 °C and reduced with hydrogen at 420 °C for 1 h. This

catalyst was 100 % active in the ESR (operation conditions: 0.1 g_{cat} with dilution and water/ethanol molar ratio = 12) at 420 °C for 30 h, the main products were H_2 (68 to 75%), CO_2 (58 to 60%) and CH_4 (41 to 35%) with traces of CO and C_2H_4O.

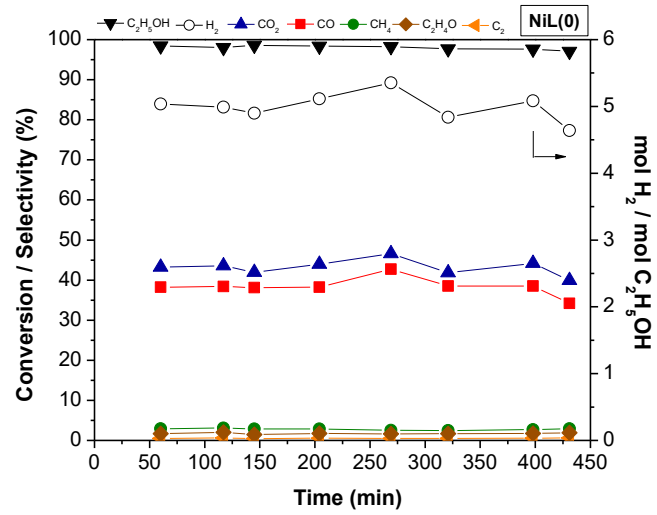

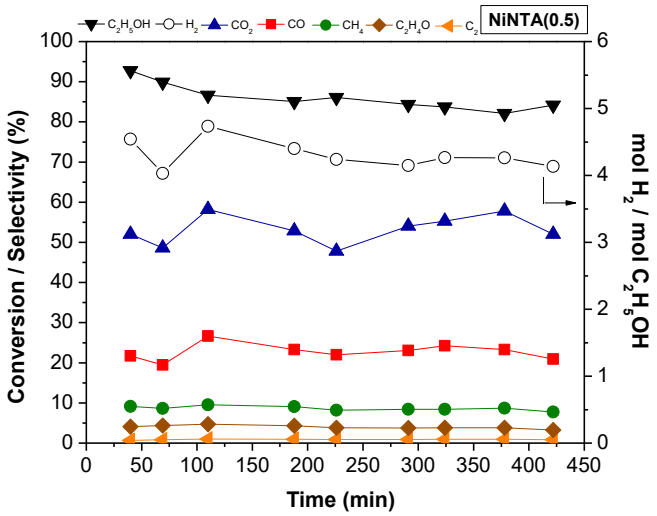

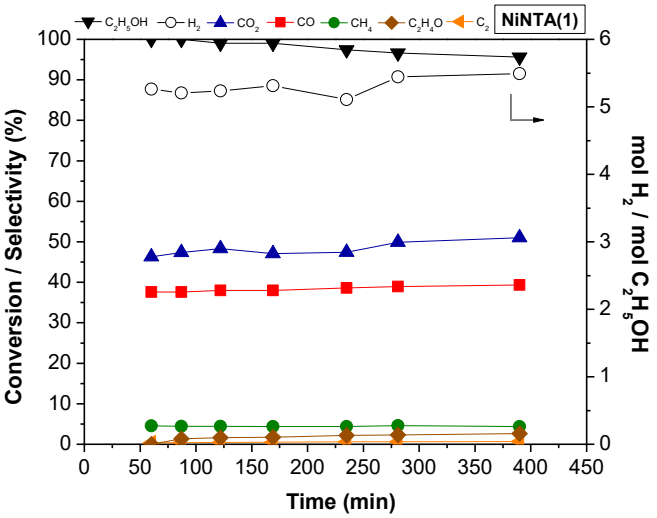

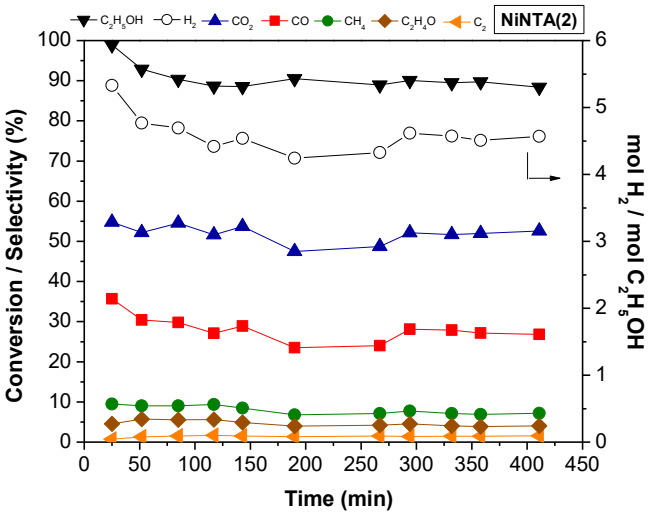
C2H5OH
H2
CO2
CO
CH4
C2H4O
C2
NiNTA(2)
Conversion / Selectivity (%)
mol H2 / mol C2H5OH
Time (min)

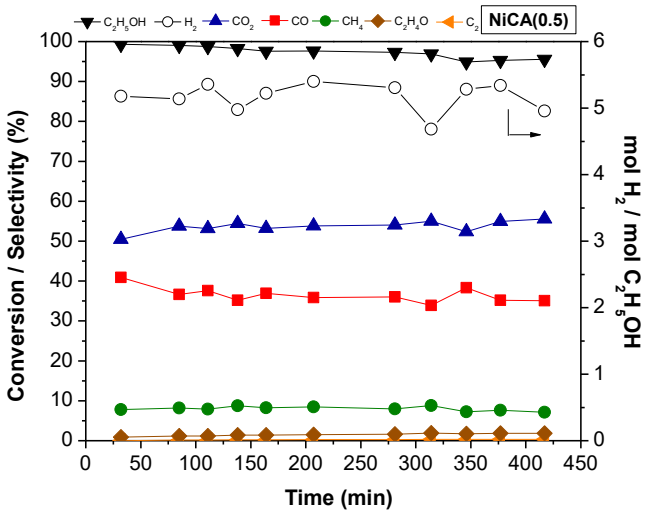
C2H5OH
H2
CO2
CO
CH4
C2H4O
C2
NiCA(0.5)
Conversion / Selectivity (%)
mol H2 / mol C2H5OH
Time (min)

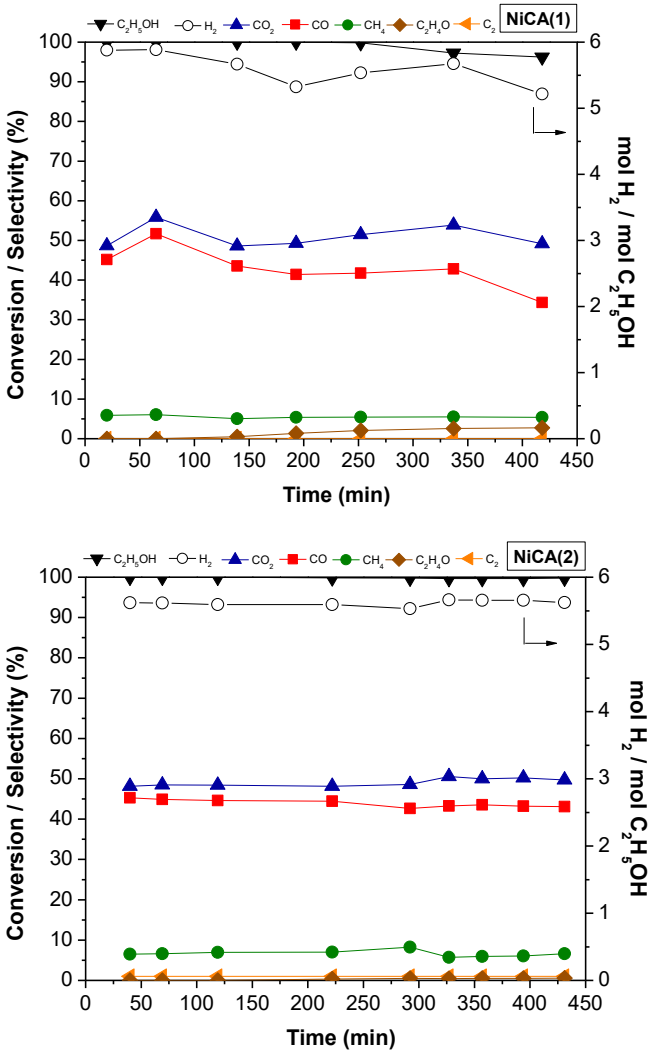

Figure 9. Ethanol conversion and product distribution in ethanol steam reforming during 7 h. T = 650 °C, $R_{H2O/C2H5OH}$ = 4.85, y_{C2H5OH} = 9.2 %.

3.5. Spent catalysts

The diffraction patterns of used catalysts are shown in Figure 10. $MgAl_2O_4$, CeO_2, NiO and Ni^0 phases are detected. The spinel and ceria are stable under the reaction conditions. The characteristic peak at 2θ = 51.8° belonging to Ni^0 is clearly detected, showing that the systems remained active during the reaction time. This peak remains broad indicating that the nickel crystallites are nano-sized even under reaction conditions. However, it is not possible to dismiss a slight sintering of the active phase. The presence of residual NiO is also observed in 2θ = 43.1° mainly in NiNTA(0.5), NiNTA(2) and NiCA(1) systems as a consequence of incomplete reduction, although no reoxidation of the active phase is ruled out. The intensity of this peak is lower than that observed in fresh samples (Figure 3), suggesting that the reduction has continued under the reactive atmosphere. NiNTA(1), NiCA(0.5) and NiCA(2) reveal less residual amount of NiO, which would indicate that these systems would have Ni^{2+} species easier to be reduced. The intensity of the characteristic graphitic carbon peak

at 2θ = 26° is higher for the NiL(0), NiNTA(0.5), NiNTA(2) and for NiCA(x>0) systems and is almost undetectable to the NiNTA(1) system.

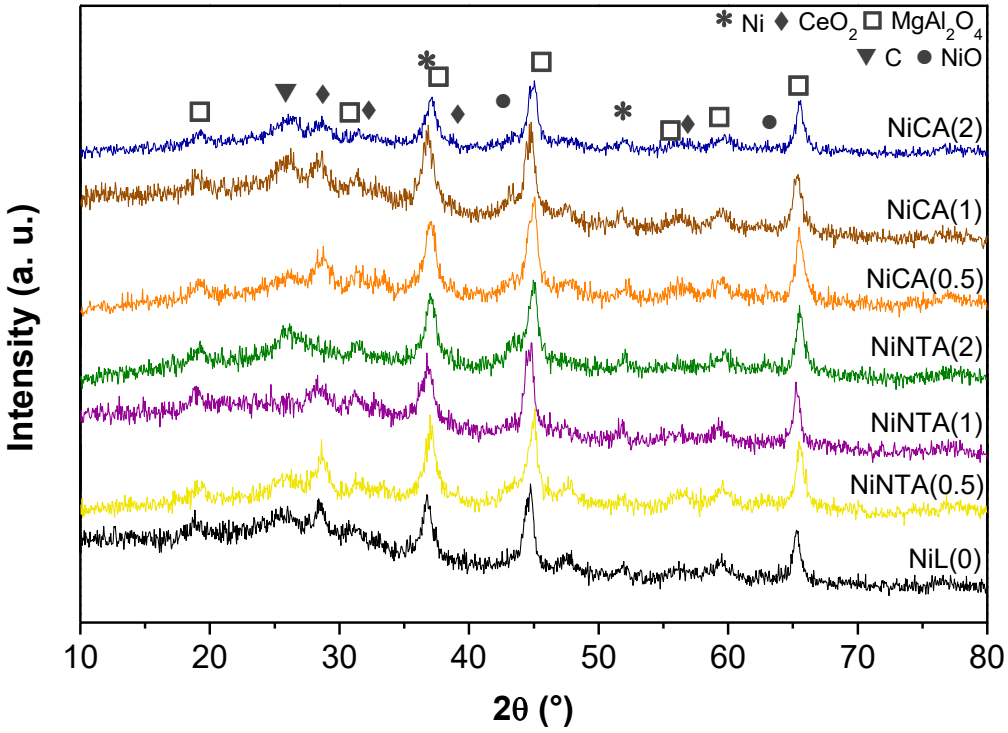

Figure 10. XRD patterns of spent catalysts after 7 h of ethanol steam reforming.

The thermograms of the catalysts used are shown in Figure S5. The weight loss of the samples under an oxidizing atmosphere mostly corresponds to the combustion of carbon deposits formed during the reforming reaction. It can be observed that the NiNTA(1) system has a small weight loss of about 2%, in accordance with those observed by XRD, Table 8. The other NTA catalysts show 32 and 35 carbon % for the NTA/Ni ratios of 0.5 and 2, respectively. The NiNTA(1) system showed larger Ni crystallite sizes than the other ones but small CeO_2 crystallite size, which enhances its oxygen release and storage properties [27] and would allow a cooperative work with Ni^0. In addition, it has a high Ce^{3+}/Ce^{4+} surface ratio and the highest Ce/Ni^0 ratio, Table 7. In the NiNTA(0.5) system, the amount of carbon can be attributed to differences in the degree of interaction between phases Ni and CeO_2, and partially related to the metal particle size. Reduced NiNTA(0.5) system presented the largest crystallite size of CeO_2 (Table 4) and low Ce^{3+}/Ce^{4+} and Ce/Ni^0. In addition, the XRD for the NiNTA(0.5) and NiNTA(2) systems reveal the presence of residual NiO, which would affect their performance in the reaction under the operation conditions used in this work. Maximum combustion temperatures of carbon deposits are lower in NTA-prepared catalysts, Table 8. Lower combustion temperatures are advantageous when considering catalyst regeneration procedures. For the NiNTA(1) system, the temperature decrease is greater than 100 °C.

In the CA-prepared systems the percentage of carbon deposited is similar in all samples. The NiCA(x>0) samples have similar properties, the main differences are related to the XPS surface ratios (Ce^{3+}/Ce^{4+} and Ce/Ni^0

ratio), Table 7. However, differences in combustion temperature are observed, associated with graphitization degree of carbon deposits. This would allow the use of a lower temperature (in the order of 50°C less) when implementing a regeneration strategy.

Table 8. Carbon amount and maximum combustion temperature from TGA-TPO of catalysts after 7 h in reaction.

Sample	**T_{max} (°C)**	**%C**	**mgC/g_{cat}h**
NiL(0)	702	22	30.6
NiNTA(0.5)	633	32	45.6
NiNTA(1)	537	~ 2	~ 1.4
NiNTA(2)	630	35	47.3
NiCA(0.5)	644	20	28.6
NiCA(1)	639	29	37.4
NiCA(2)	653	28	37.7

The Raman spectra of NiNTA(x) and NiCA(x) systems are shown in Figure 11. The Raman spectra of the first-order region correspond to carbonaceous zone on the catalysts [73]. These spectra were deconvolutioned in five contributions according to reported by Sadezky et al. [74]. The deconvolution of the spectra was performed using Lorentzian curves for G, D1, D2 and D4 contributions and using Gaussian curve for D3 contribution. The G band around 1580 cm^{-1} is associated with the E_{2g} optical mode of graphite or sp^2 carbon materials [75]. The D bands are characteristic for disordered graphite and its intensity relative to the G band increase with increasing degree of disorder in the graphitic structure [74]. The D1 band around 1340 cm^{-1} corresponds to a graphitic lattice vibration mode with A_{1g} symmetry [74]. The I_{D1}/I_G ratio increases with the amount of disorder [76]. The band positions and Raman ratios are shown in Table 9. The I_{D1}/I_G intensity ratio were higher for the NiNTA(x) and NiCA(x) systems. Then, it could be inferred that the use of chelating agents (NTA or CA) increases the amount of disorder on the carbonaceous deposits and it is also related to decrease of temperature of combustion, Table 8, indicating that the carbon with a major disorder burns at less temperature. A shift in G band positions is observed when NTA or CA were used in the catalyst preparation, suggesting smaller crystallite sizes of the formed graphite-like carbon [77].

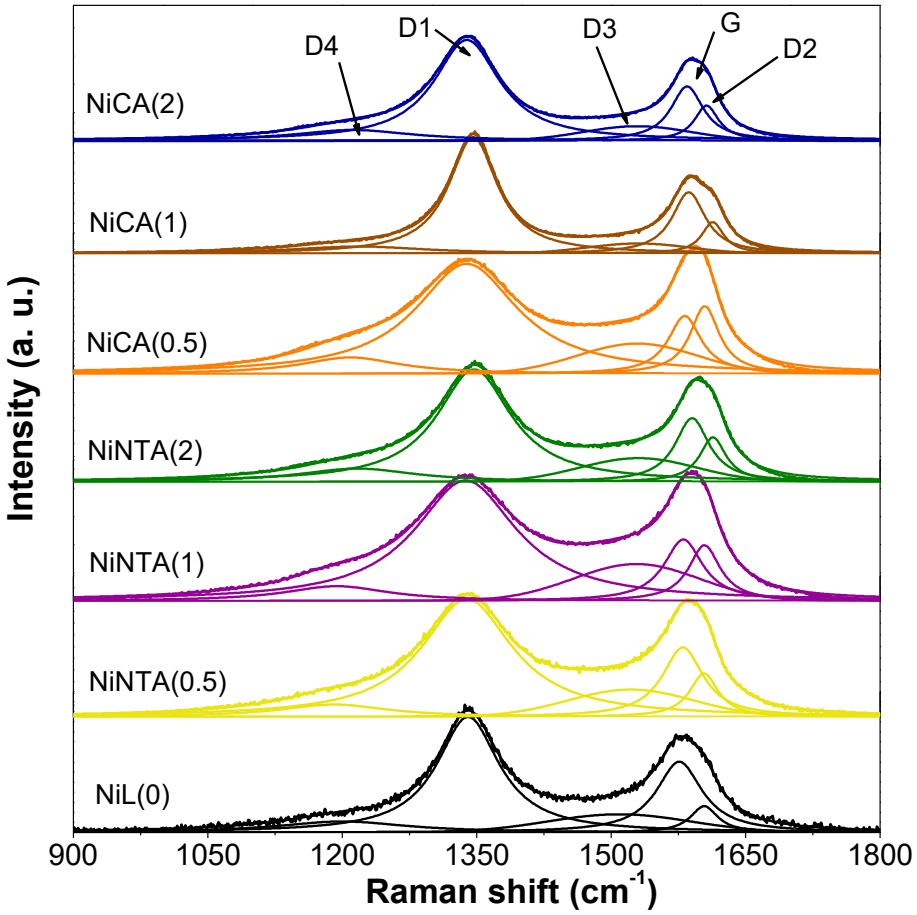

Figure 11. Raman spectra of used catalysts after 7 h in ethanol steam reforming.

Table 9. Raman band positions and I_{D1}/I_G ratio for used catalysts.

Sample	Raman shift (cm^{-1})					I_{D1}/I_G	I_{D3}/I_G
	G	D1	D2	D3	D4		
NiL(0)	1576	1340	1603	1508	1200	1.63	0.53
NiNTA(0.5)	1580	1339	1604	1522	1191	1.70	0.80
NiNTA(1)	1581	1338	1604	1528	1194	1.96	1.29
NiNTA(2)	1590	1347	1614	1530	1217	1.76	0.84
NiCA(0.5)	1582	1338	1604	1529	1209	1.90	1.25
NiCA(1)	1587	1346	1613	1530	1218	1.90	0.34
NiCA(2)	1585	1339	1606	1529	1212	1.85	0.58

The carbon deposition was also examined by SEM. All SEM images of the catalysts show two zones, Figure 12: (i) one with almost negligible amount of carbon deposits and (ii) other with an abundant deposition od carbon, [78-80]. This clearly reveals that carbon deposition is not homogeneous regardless of the precursor used in the synthesis of catalysts. SEM images of NiNTA(0.5) and NiNTA(2) show zones with a abundant amount

of filaments of different sizes and carbon free regions. For NiNTA(1), the carbon deposits appears to be amorphous carbon type, in agreement with the high I_{D3}/I_G ratio, Table 9 [74]. The I_{D3}/I_G ratios for NiCA(x>0) systems are also high, however only filamentous-type carbon deposits were observed by SEM. For NiCA(1) catalyst, the carbon filaments seem to be longer. The carbon type is also related to the presence of secundary products.

Nickel signal is clearly detected by EDX in the carbon regions for all catalysts, which allows to infer that the metal particle could be at the end of the filaments, which is very common in nickel catalysts. The presence of areas with and without carbon makes it possible to assume that their deposition is associated with the presence of metal particles and that the bare support does not mostly contribute to the deposition mechanism or the occurrence of secondary reactions.

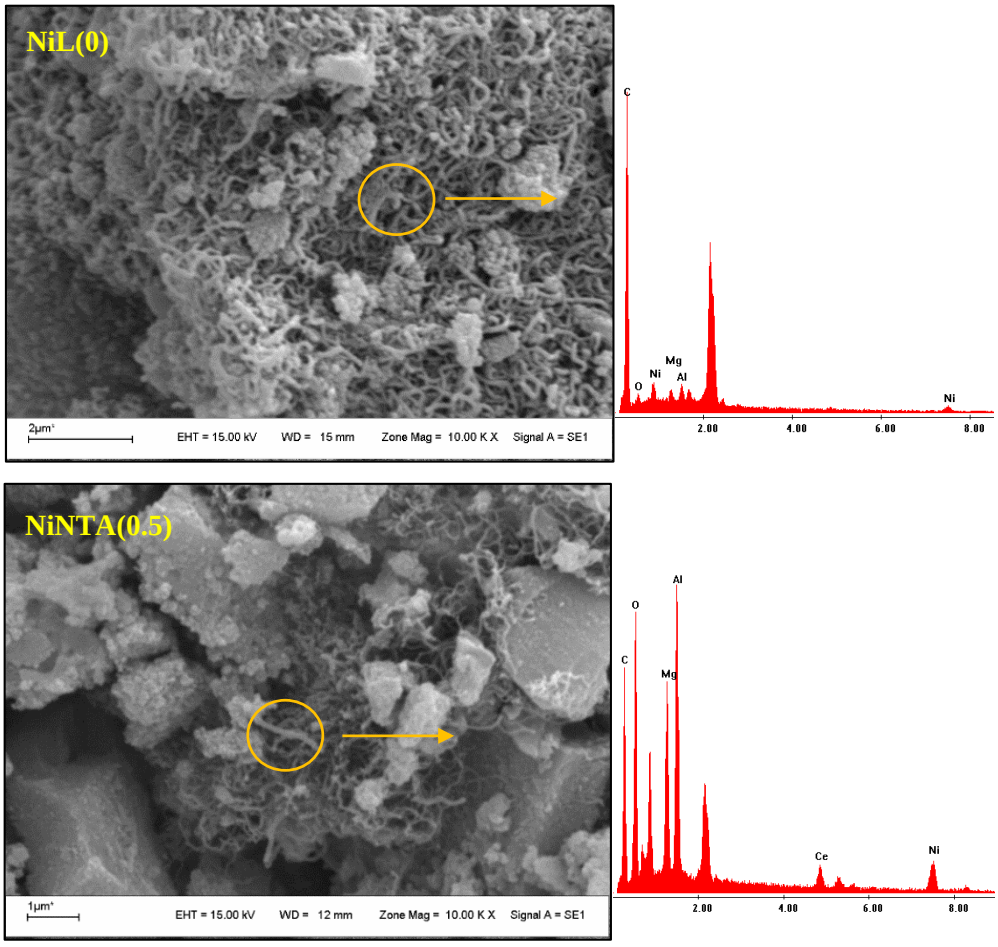

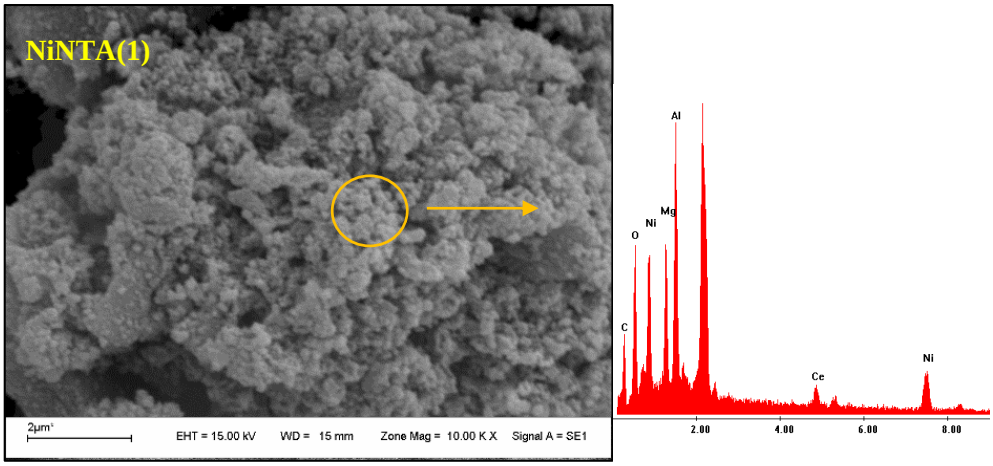
NiNTA(1)
2µm*
EHT = 15.00 kV
WD = 15 mm
Zone Mag = 10.00 K X
Signal A = SE1
C
O
Ni
Mg
Al
Ce
Ni
2.00
4.00
6.00
8.00

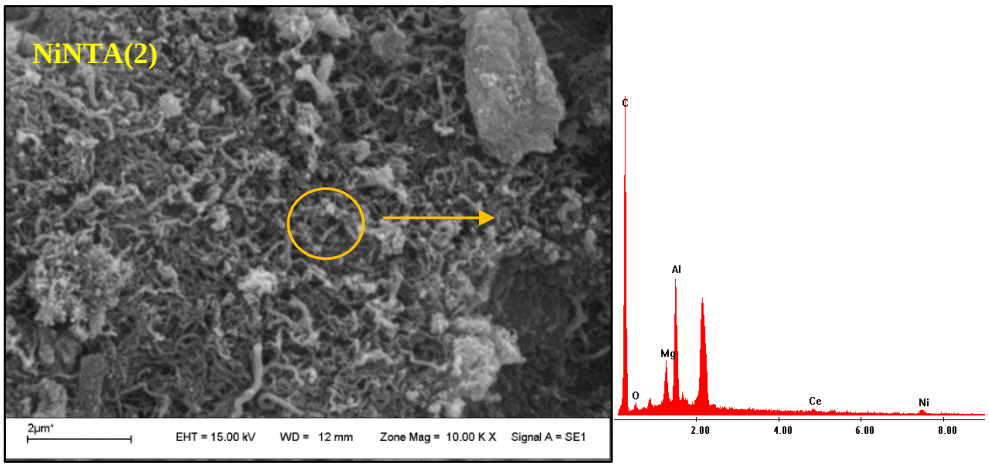
NiNTA(2)
2µm*
EHT = 15.00 kV
WD = 12 mm
Zone Mag = 10.00 K X
Signal A = SE1
C
O
Mg
Al
Ce
Ni
2.00
4.00
6.00
8.00

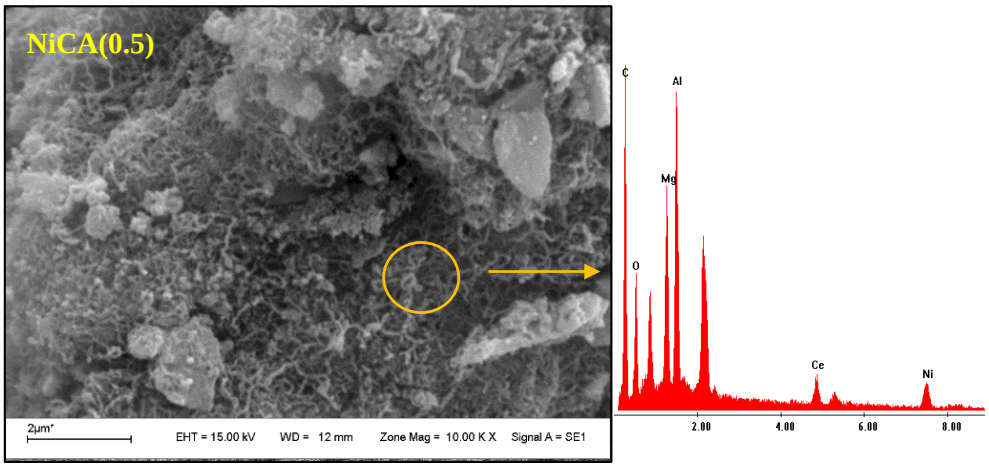
NiCA(0.5)
2µm*
EHT = 15.00 kV
WD = 12 mm
Zone Mag = 10.00 K X
Signal A = SE1
C
O
Mg
Al
Ce
Ni
2.00
4.00
6.00
8.00

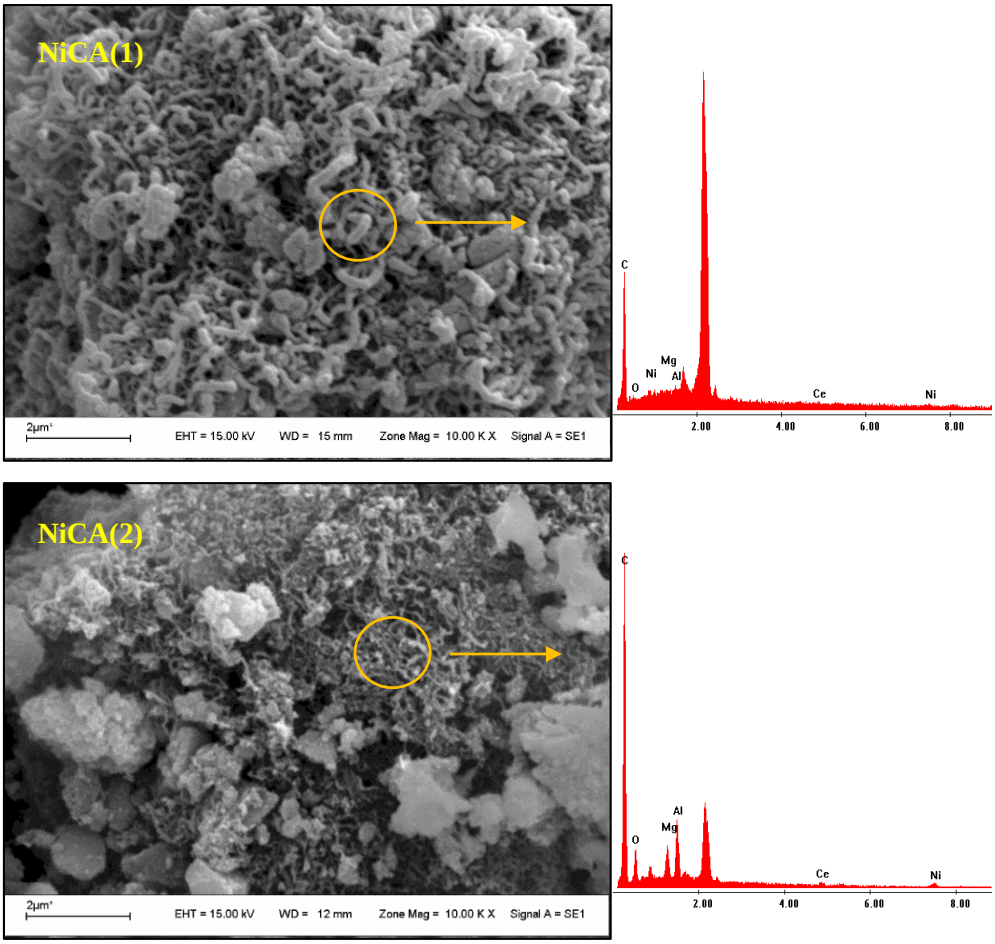

Figure 12. SEM images and EDX spectra of spent catalysts after 7 h of ethanol steam reforming.

4. Conclusions

The catalytic performance of a series of Ni/$MgAl_2O_4$-CeO_2 catalysts were tested in ethanol steam reforming reaction. The catalysts were prepared by the wet impregnation method using L: NTA or CA as chelating agents. The influence of different L/Ni molar ratios was studied.

In all dried samples the presence of some complex species L-Ni on the support surface was verified. However, in the calcined samples, Ni^{2+} species were in an octahedral environment similar to NiO without a significant amount of carbon residues from the chelanting agent. The changes in surface properties of catalysts were be associated to a memory effect.

Improved interactions among NiO-CeO_2 and Ni-CeO_2 were obtained by the use of chelating agents. These interactions were revealed by HRTEM images, the behavior under reduction condictions and the increase in the Ce/Ni^0 surface ratio.

The NTA addition in the preparation of catalytic systems allowed to decrease the NiO crystallite sizes. After reduction, the Ni^0 crystallite sizes were smaller for NiNTA(0.5) and NiNTA(2) systems. Due to the redissolution

of the ceria during impregnation with solutions containing Ni^{2+} and NTA, the crystallite size of CeO_2 was also affected, mainly with a molar ratio NTA/Ni =1 and 2.

The CA addition in the preparation of Ni catalysts promoted the formation of smaller NiO and Ni^0 crystallite sizes, with a slight effect on the size of CeO_2 particles.

The catalysts prepared with a molar ratio NTA/Ni=1 and CA/Ni=2 exhibited better catalytic performances in the ethanol reforming reaction under the operation conditions used. The NiNTA(1) and NiCA(2) system presented high Ce/Ni^0 surface ratios. The NiNTA(1) showed a high tolerance to carbon deposition while no improvement in tolerance to carbon deposition was observed for NiCA(2). The use of chelantig agents in catalysts preparation induced changes in the type of carbon. The carbon removal through oxidation in catalysts prepared using NTA or CA requires lower temperatures, which is beneficial for implementing a regeneration strategy. Although all the NiL(x) systems showed a good catalytic performance in ethanol steam reforming, under the experimental conditions used, the best performance in term of hydrogen production were obtained with NiNTA(1) and NiCA(2) systems. These systems were prepared using the stoichiometric molar ratios to form the most stable complex in solution between nickel and chelating agent.

Acknowledgments

Financial supports are acknowledged to CONICET (PIP 00327/CO and PIP 00227/CO) and Universidad Nacional de San Luis (PROICO 2-0116). The authors are grateful to ANPCyT for Grant PME 8-2003 to finance the purchase of the UHV Multi Analysis System. JL is a Serra Húnter fellow and is grateful to ICREA Academia program and projects MICINN/FEDER RTI2018-093996-B-C31 and GC 2017 SGR 128.

References

[1] S. Ogo, Y. Sekine; Fuel Processing Technology 199 (2020) 106238
[2] Q. Zhang, K. Long, J. Wang, T. Zhang, Z. Song, Q. Lin; Inter. J. Hydro. Energy 42 (2017) 14103-14114
[3] J. L. Contreras, J. Salmones, J. A. Colıín-Luna, L. Nuño, B. Quintana, I. Córdova, B. Zeifert, C. Tapia, G. A. Fuentes, *I. J. Hyd. Energy* 39 (2014) 18835.
[4] S. Bepari, D. Kuila; International Journal of Hydrogen Energy 45 (2020) 18090-18113.
[5] C. Montero, A. Remiro, B. Valle, L. Oar-Arteta, J. Bilbao, A. G. Gayubo; Ind. Eng. Chem. Res. 2019, 58, 14736−14751
[6] J. R. Rostrup-Nielsen, J. Sehested, J. Norskov, *Adv. Catal.* 47 (2002) 65
[7] Y. C. Sharma, A. Kumar, R. Prasad, S. N. Upadhyay; *Renew. Sust. Energ. Rev*. 74 (2017) 89-103.
[8] L. V. Mattos, G. Jacobs, B. H. Davis, F. B. Noronha, *Chem. Rev.* 112 (2012) 4094.
[9] A. J. van Dillen, R. Terorde, D. Lensveld, J. Geus, K. de Jong; *J. Catal*. 216 (2003) 257-264
[10] Umar C. Abubakar, Khalid R. Alhooshani, Tawfik A. Saleh; Journal of Environmental Chemical Engineering 8 (2020) 103811.
[11] J. Escobar, M.C. Barrera, J.A. de los Reyes, J.A. Toledo, V. Santes, J.A. Colin; *J. Mol. Catal*. A 287 (2008) 33-40.
[12] T. Shimizu, K. Hiroshima, T. Honma, T. Mochizuki, M. Yamada; *Catal. Today* 45 (1998) 271-276.
[13] T. Mochizuki, T. Hara, N. Koizumi, M. Yamada; *Appl. Catal. A* 317 (2007) 97-104.

[14] J-S. Girardon, E. Quinet, A. Griboval-Constant, P.A. Chernavskii, L. Gengembre, A.Y. Khodakov; *J. Catal*. 248 (2007) 143–157.
[15] S. Karnjanakom, G. Guan, B. Asep, X. Dua, X. Hao, C. Samart, A. Abudula; *Energy Conv. Manag*. 98 (2015) 359–368.
[16] X. Lu, Jian-Feng Chen, Y.Tan, Y. Zhang; *Catal. Comm*. 20 (2012) 6–11.
[17] Y. Bang, S. Park, S-J Han, J. Yoo, J-H Song, J. H Choi, K. H. Kang, I. K. Song; *Appl. Catal. B* 180 (2016) 179-188.
[18] K. Al-Dalama, B. Aravind y A. Stanislaus; Appl. Catal., A 296 (2005) 49-53.
[19] G. Słowik, M. Greluk, M. Rotko, A. Machocki; Applied Catalysis B: Environmental 221 (2018) 490–509.
[20] C. Wu, P. T. Williams; Applied Catalysis B: Environmental 102 (2011) 251–259
[21] J. Ryczkowski, W. Grzegorczyk, D. Nazimek; Appl. Catal. A 126 (1995) 341-349.
[22] G. Anderegg; *Pure Appl. Chem.* 54 (1982) 2693-2758. W. Hummel, G. Anderegg, L. Rao, I. Puigdomènech, O. Tochiyama; *Chemical thermodynamics of compounds and complexes of U, Np, Pu, Am, Tc, Se, Ni and Zr with selected organic ligands*, USA, Elsevier Science, 2005.
[23] A.E. Galetti, M.F. Gomez, L.A. Arrúa, M.C. Abello Applied Catalysis A: General 348 (2008) 94–102
[24] A. Trovarelli, J. Llorca; *ACS Catal.* 7 (2017) 4716.
[25] L. Soler, A. Casanovas, J. Ryan, I. Angurell, C. Escudero,V. Pérez-Dieste, J. Llorca; *ACS Catalysis* 9 (2019) 3641-3647.
[26] T. Montini, M. Melchionna, M. Monai, P. Fornasiero; *Chem. Rev*. 116 (2016) 5987
[27] A. Elmhamdi, R. Castañeda, A. Kubacka, K. Nahdi, A. Martínez, *Appl. Catal. B* 188 (2016) 292.
[28] A.C. Villagrán-Olivares, M.F. Gomez, M.N. Barroso, M.C. Abello; Molecular Catalysis 481 (2020) 110164
[29] A. Villagrán-Olivares, M. F. Gomez, C. López, M. N. Barroso, M. C. Abello. Applied Catalysis B: Environmental 264 (2020) 118510
[30] H. M. Rietveld; J. Appl. Crystallogr 2 (1969) 65–71.
[31] J. Rodríguez-Carvajal; Phys. B Condens. Matter 192 (1993) 55–69.
[32] P. Thompson, D. E. Cox, J. B. Hastings; *J. Appl. Crystallogr.* 20 (1987) 79–83.
[33] J. R. H. Ross (2019); Catalyst Characterization. Contemporary Catalysis, 121–132. doi:10.1016/b978-0-444-63474-0.00005-9
[34] I. Puigdomenech, Medusa software, Chem. Equilibr. Diagrams 2 (2013), https://www.kth.se/en/che/medusa/downloads-1.386254.
[35] L. Bonneviot, O. Legendre, M. Kermarec, D. Olivier, M. Che; *J. Colloid Interf. Sci.* 134 (1990) 534-547.
[36] G. George, S. Anandhan; *RSC Adv.* 4 (2014) 62009–62020
[37] V. A. Suárez-Toriello, C. E. Santolalla-Vargas, J. A. de los Reyes, A. Vázquez-Zavala, M. Vrinat, C. Geantet; *J. Mol. Catal. A* 404–405 (2015) 36–46.
[38] J. Calvache-Muñoz, F. A. Prado, J. E. Rodríguez-Páez; *Colloids Surf. A* 529 (2017) 146-159.
[39] Z. Yu, X. Hu, P. Jia, Z. Zhang, D. Dong, G. Hu, S. Hu, Y. Wang, J. Xiang; *Appl. Catal. B* 237 (2018) 538–553.
[40] K. Q. Sun, E. Marceau y M. Che; *Phys. Chem. Chem. Phys.* 8 (2006) 1731-1738.
[41] R. A. Ortega-Domínguez, H. Vargas-Villagrán, C. Peñaloza-Orta, K. Saavedra-Rubio, X. Bokhimi, T. E. Klimova; *Fuel* 198 (2017) 110–122.
[42] N. Koizumi, Y. Ibi, D. Hongo, Y. Hamabe, S. Suzuki, Y. Hayasaka, T. Shindo, M. Yamada; J. Catal. 289 (2012) 151-163
[43] L. Espinosa-Alonso, K. P. de Jong, B. M. Weckhuysen; *J. Phys. Chem. C* 112 (2008) 7201-7209.
[44] L. Y. Wang, G. Q. Wu, D. G. Evans; *Mater. Chem. Phys.* 104 (2007) 133-140.
[45] S. Bepari, S. Basu, N. Pradhan, A. K. Dalai; *Catal. Today* 291 (2017) 47-57.
[46] G. Sócrates; *Infrared and Raman Characteristic Group Frequencies: Tables and Charts.* 3ra Edición, J. Wiley and Sons, 2001. ISBN: 0-471-85298-8. K. Nakamoto; *Infrared and Raman Spectra of Inorganic and Coordination Compounds*, 4ta Edición, John Wiley and Sons 1986, pages 232-239
[47] O. Gyliene, J. Aikaite, O. Nivinskiene; *J. Hazard Mater.* 109 (2004) 105-111.
[48] K. A. Tarasov, D. O´Hare; *Inorg. Chem.* 42 (2003) 1919-1927.
[49] F. Wypych, G. G. Carbajal Arízaga, J. E. Ferreira da Costa Gardolinski; *Journal of Colloid and Interface Science* 283 (2005) 130–138
[50] W. Brockner, C. Ehrhardt, M. Gjikaj; *Thermochim. Acta* 456 (2007) 64–68.
[51] G. Leofanti, M. Padovan, G. Tozzola, B. Venturelli; *Catal. Today* 41 (1998) 207-219

[52] S. A. Theofanidis, V. V. Galvita, H. Poelman, R. Batchu, L. C. Buelens, C. Detavernier, G. B. Marin; *Appl. Catal. B* 239 (2018) 502-512
[53] M. Zarei, F. Meshkani, M. Rezaei; *Adv. Powder Technol.* 27 (2016) 1963–1970.
[54] C. E. Santolalla-Vargas, V. A. Suárez Toriello, J. A. de los Reyes, D. K. Cromwell, B. Pawelec, J. L. G. Fierro; *Mater. Chem. Phys.* 166 (2015) 105-115
[55] K. Y. Koo, S.-h. Lee, U. H. Jung, H.-S. Roh, W. L. Yoon; *Fuel Process. Technol.* 119 (2014) 151-157
[56] B. Li, X. Qian, X. Wang; *I. J. Hydrogen Energ.* 40 (2015) 8081-8092
[57] R. Jalali, B. Nematollahi, M. Rezaei, M. Baghalha; *I. J. Hydrogen Energ.* 44 (2019) 10427-10442.
[58] S. Damyanova, B. Pawelec, R. Palcheva, Y. Karakirova, M. C. Capel Sanchez, G. Tyuliev, E. Gaigneaux, J. L. G. Fierro; *Appl. Catal. B* 225 (2018) 340-353.
[59] J. A. Santander, G. M. Tonetto, M. N. Pedernera, E. López; *I. J. Hydrogen Energ.* 42 (2017) 9482-9492.
[60] A. Ebadi, S. Tourani, F. Khorasheh; *Ind. Eng. Chem. Res.* 57 (2018) 12700−12714.
[61] A. Di Michele, A. Dell'Angelo, A. Tripodi, E. Bahadori, F. Sánchez, D. Motta, N. Dimitratos, I. Rossetti, G. Ramis; *I. J. Hydrogen Energ.* 44 (2019) 952-964.
[62] M. Li, X. Wang, S. Li, S. Wang, X. Ma; *I. J. Hydrogen Energ.* 35 (2010) 6699-6708.
[63] M. Chen, Y. Wang, Z. Yang, T. Liang, S. Liu, Z. Zhou, X. Li; *Fuel* 220 (2018) 32–46.
[64] S. C. M. Mizuno, A. H. Braga, C. E. Hori, J. B. O. Santos, J. M. C. Bueno; *Catal. Today* 296 (2017) 144–153.
[65] L. Jalowiecki-Duhamel, C. Pirez, M. Capron, F. Dumeignil, E. Payen; *I. J. Hydrogen Energ.* 35 (2010) 12741-12750.
[66] R. Yang, X. Li, J. Wu, X. Zhang, Z. Zhang, Y. Cheng, J. Guo; *Appl. Catal A* 368 (2009) 105-112.
[67] K.-Q. Sun, E. Marceau, M. Che; Phys. Chem. Chem. Phys., 2006, 8, 1731–1738.
[68] A. Iriondo et al. International Journal of Hydrogen Energy 35 (2010) 11622-11633.
[69] E. Varga, Z. Ferencz, A. Oszkó, A. Erdphelyi, J. Kiss; J. Mol. Catal A 397 (2015) 127-133.
[70] J. W. C. Liberatori, R. U. Ribeiro, D. Zanchet, F. B. Noronha, J. M. C. Bueno; Appl. Catal. A 327 (2007) 197-204.
[71] J. Chen, D. Xu; Int. J. Sustain. Green Energ. 6 (2017) 28-38.
[72] F. Haga, T. Nakajima, H. Miya, S. Mishima; Catal. Lett. 48 (1997) 223-227.
[73] M. Pawlyta, J.-N. Rouzaud, S. Duber; Carbon 84 (2015) 479-490
[74] A. Sadezky, H. Muckenhuber, H. Grothe, R. Niessner, U. Pöschl; Carbon 43 (2005) 1731–1742
[75] J. McGregor, Z. Huang, Edward P.J. Parrott, J. Axel Zeitler, K. Lien Nguyen, Jeremy M. Rawson, Albert Carley, Thomas W. Hansen, Jean-Philippe Tessonnier, Dang Sheng Su, Detre Teschner, Elaine M. Vass, Axel Knop-Gericke, R. Schlögl, Lynn F. Gladden; Journal of Catalysis 269 (2010) 329–339
[76] L. Bokobza, J.-L. Bruneel, M. Couzi, Carbon (2015) 77-94.
[77] H.-Z. Wang, L.-L. Sun, Z.-J. Sui, Y.-A. Zhu, G.-H. Ye, D. Chen, X.-G. Zhou, W.-K. Yuan; Ind. Eng. Chem. Beef. 57 (2018) 8647-8654.
[78] A.C. Villagrán Olivares, M. N. Barroso, M. F. Gomez, M. C. Abello; International Journal of Industrial Chemistry 9 (2018) 61-73.
[79] M. N. Barroso, M. F. Gomez, L. A. Arrúa, M. C. Abello; International Journal of Hydrogen Energy 39 (2014) 8712-8719.
[80] A. E. Galetti, M. F. Gomez, L. A. Arrua, M. C. Abello; Applied Catalysis A: General 408 (2011) 78– 86

Supplementary material

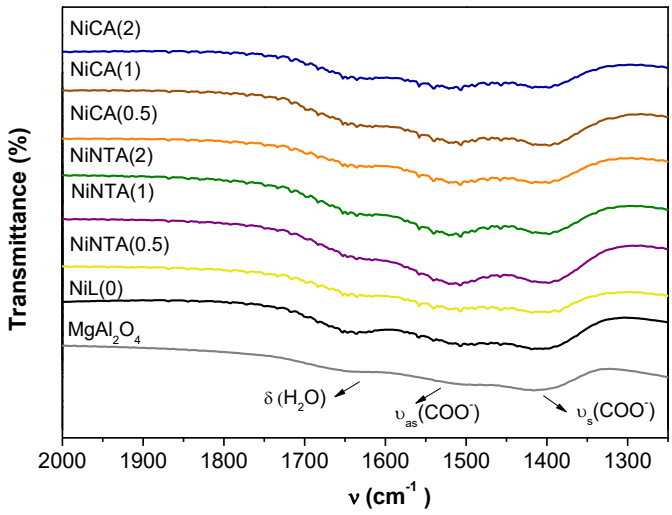

Figure S1. Infrared spectra of fresh catalysts.

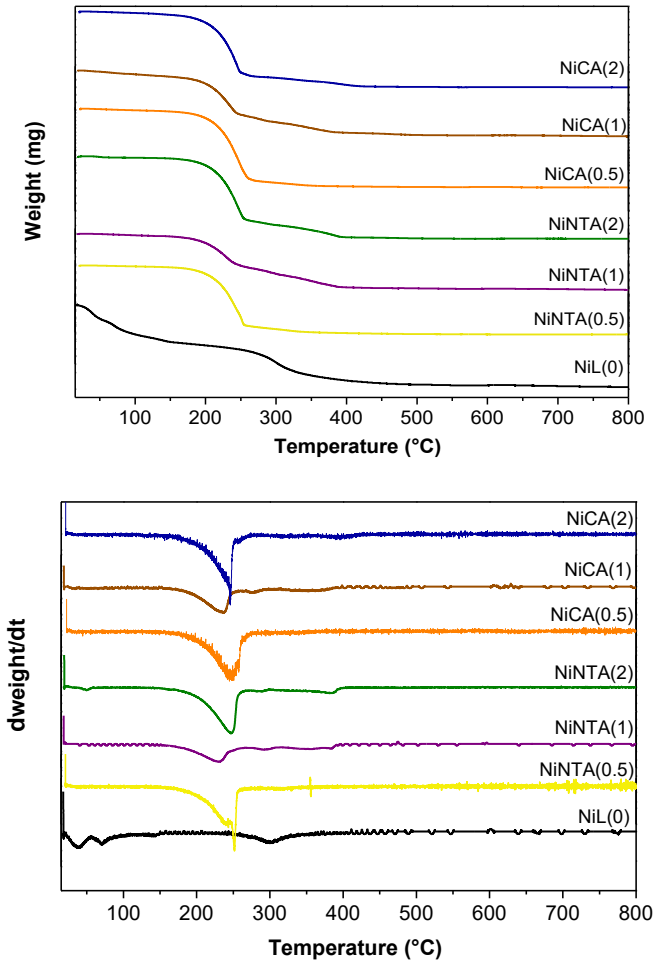

Figure S2. Thermograms and dweight/dt vs. temperature of dried catalysts.

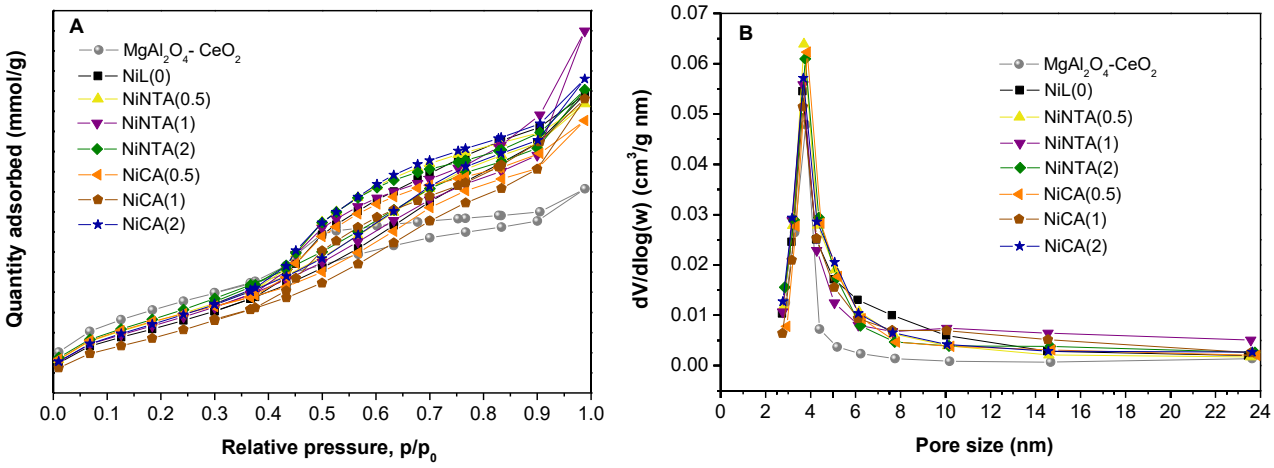

Figure S3. N_2 adsorption-desorption isotherms (A) and porous size distribution (B) of fresh catalysts.

Table S1. TGA results of precursor decomposition.

Sample	Teoric reaction of decomposition	Theorical weight loss (%)	Experimental weight loss (%)
NiL(0)	$Ni(NO_3)_2 \rightarrow NiO + gas$	59.1	37.8
NiNTA(0.5)	$0.5\ Ni(NO_3)_2 + 0.5\ [NiNTA]^- \rightarrow NiO + gas$	65.2	69.7
NiNTA(1)	$[NiNTA]^- \rightarrow NiO + gas$	69.7	56.6
NiNTA(2)	$[Ni(NTA)_2]^{4-} \rightarrow NiO + gas$	82.8	76.7
NiCA(0.5)	$0.5\ Ni(NO_3)_2 + 0.5\ [NiCA]^- \rightarrow NiO + gas$	65.3	75.4
NiCA(1)	$[NiCA]^- \rightarrow NiO + gas$	69.8	63.7
NiCA(2)	$[Ni(CA)_2]^{4-} \rightarrow NiO + gas$	83.9	76.3

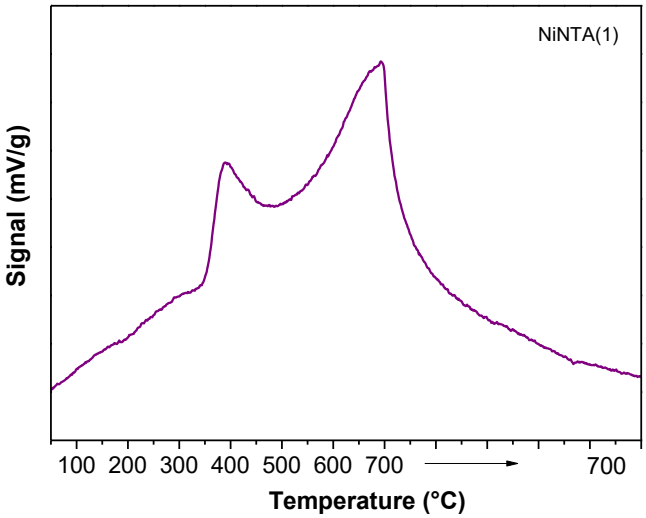

Figure S4. TPR profile of NiNTA(1) (automatic Micromeritics AutoChem II equipment).

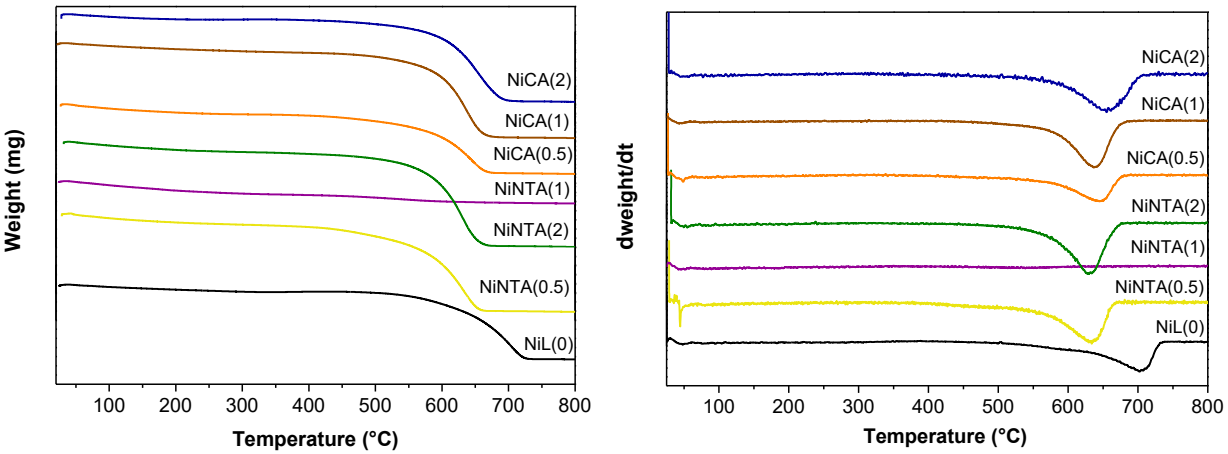

Figure S5. Thermograms and dweight/dt vs. temperature of used catalysts after 7 h of reaction.